Received: 17 December 2021 | Revised: 29 May 2022 | Accepted: 8 June 2022

DOI: 10.1002/hipo.23451

RESEARCH ARTICLE

WILEY

Complementary representations of time in the prefrontal cortex and hippocampus

Wing Ning[1,2,3] | John H. Bladon[1,2,4] | Michael E. Hasselmo[1,2]

[1]Center for Systems Neuroscience, Boston University, Boston, Massachusetts, USA

[2]Department of Psychological and Brain Sciences, Boston University, Boston, Massachusetts, USA

[3]Department of Neurobiology and Behavior, University of California, Irvine, Irvine, California, USA

[4]Department of Psychology, Brandeis University, Waltham, Massachusetts, USA

Correspondence
Wing Ning, Center for Systems Neuroscience, Boston University, 610 Commonwealth Avenue, Boston, MA 02215, USA.
Email: wingning@bu.edu

John H. Bladon, Center for Systems Neuroscience, Boston University, 610 Commonwealth Avenue, Boston, MA 02215, USA.
Email: jhbladon@bu.edu

Funding information
U.S. National Institutes of Health, Grant/Award Numbers: R01 MH052090, R01 MH060013, R01 MH095297, R01 MH120073; U.S. Office of Naval Research, Grant/Award Numbers: DURIP N00014-17-1-2304, MURI N00014-16-1-2832, MURI N00014-19-1-2571

Abstract

Episodic memory binds the spatial and temporal relationships between the elements of experience. The hippocampus encodes space through place cells that fire at specific spatial locations. Similarly, time cells fire sequentially at specific time points within a temporally organized experience. Recent studies in rodents, monkeys, and humans have identified time cells with discrete firing fields and cells with monotonically changing activity in supporting the temporal organization of events across multiple timescales. Using in vivo electrophysiological tetrode recordings, we simultaneously recorded neurons from the prefrontal cortex and dorsal CA1 of the hippocampus while rats performed a delayed match to sample task. During the treadmill mnemonic delay, hippocampal time cells exhibited sparser firing fields with decreasing resolution over time, consistent with previous results. In comparison, temporally modulated cells in the prefrontal cortex showed more monotonically changing firing rates, ramping up or decaying with the passage of time, and exhibited greater temporal precision for Bayesian decoding of time at long time lags. These time cells show exquisite temporal resolution both in their firing fields and in the fine timing of spikes relative to the phase of theta oscillations. Here, we report evidence of theta phase precession in both the prefrontal cortex and hippocampus during the temporal delay, however, hippocampal cells exhibited steeper phase precession slopes and more punctate time fields. To disentangle whether time cell activity reflects elapsed time or distance traveled, we varied the treadmill running speed on each trial. While many neurons contained multiplexed representations of time and distance, both regions were more strongly influenced by time than distance. Overall, these results demonstrate the flexible integration of spatiotemporal dimensions and reveal complementary representations of time in the prefrontal cortex and hippocampus in supporting memory-guided behavior.

KEYWORDS
episodic memory, hippocampus, in vivo electrophysiology, prefrontal cortex, theta phase precession, time cells

Wing Ning and John H. Bladon shared equally to the first authorship.

1 | INTRODUCTION

Episodic memory requires the ability to effectively remember the time and location of events (Eichenbaum & Fortin, 2003; Hasselmo, 2012; Tulving, 1983). Models of episodic memory commonly include interactions of storage mechanisms in the hippocampus (HPC) with the regulation of encoding and retrieval by the prefrontal cortex (PFC) (Eichenbaum, 2017b; Hasselmo & Eichenbaum, 2005). As a locus for memory, spiking activity in the hippocampus could provide a neural substrate for coding location and time based on the response of place cells (O'Keefe & Burgess, 2005; O'Keefe & Dostrovsky, 1971; O'Keefe & Recce, 1993) as well as time cells that fire at specific temporal intervals during running in one location (Kraus et al., 2013; MacDonald et al., 2011, 2013; Mau et al., 2018; Pastalkova et al., 2008; Shimbo et al., 2021; Taxidis et al., 2020). Time cell sequences have been observed in other structures, including the prefrontal cortex (Bakhurin et al., 2017; Cruzado et al., 2020; Pilkiw & Takehara-Nishiuchi, 2018; Tiganj et al., 2017), medial entorhinal cortex (Kraus et al., 2015), and striatum (Akhlaghpour et al., 2016; Bakhurin et al., 2017; Mello et al., 2015). In contrast, neuronal responses also show ramping activity with gradual increases or decreases in firing over an extended delay period in the hippocampus and subiculum (Deadwyler & Hampson, 2004; Hampson & Deadwyler, 2003), during the expectation of reward in the striatum (van der Meer & Redish, 2011), during interval timing and working memory in the prefrontal cortex (Kim et al., 2013), and during exploration of different environments in the lateral entorhinal cortex (Tsao et al., 2018). Previous studies independently compared activity in the prefrontal cortex and hippocampus under different behavioral task demands so how these two complementary, distributed representations support temporal coding remain unclear. To rule out confounding factors, here we utilized simultaneous tetrode recordings to directly compare the neural coding of time in the prefrontal cortex and hippocampus during the treadmill period of a delayed match to sample task.

Hippocampal neurons also show temporal coding of behavioral variables in terms of spiking relative to the phase of theta rhythm oscillations in the local field potential (LFP). Place cells exhibit theta phase precession, a transition in the firing phase from late phases to early phases as an animal traverses the place field (Kjelstrup et al., 2008; O'Keefe & Recce, 1993; Skaggs et al., 1996), with a slope that changes with the size of place fields or running speed (Huxter et al., 2003; Kjelstrup et al., 2008; Maurer et al., 2012; Skaggs et al., 1996). Time cells also show theta phase precession as animals pass through the temporal firing field (Pastalkova et al., 2008; Shimbo et al., 2021). Time cell responses have been modeled based on an inverse Laplace transform that can combine ramping cells with exponential decays to generate time cells that peak at discrete times (Howard et al., 2014; Liu et al., 2019; Shankar et al., 2016). These computational models provide a framework for the prediction of the time of future events on different time scales (Shankar et al., 2016), and this predictive model can simulate theta phase precession in both discrete time cells (Pastalkova et al., 2008) and ramping cells (van der Meer & Redish, 2011). Consistent with this multi-scale representation, theta phase precession has been shown to change slope when animals run through firing fields of different sizes regardless of running speed (Kjelstrup et al., 2008), and can show slow precession during ramp-like changes in firing rate (Terada et al., 2017; van der Meer & Redish, 2011). Some neurons with broader firing fields can show multiple cycles of precession during a broadly distributed increase in firing rate over locations (Kim et al., 2012; Skaggs et al., 1996). In the current work, we investigate phase coding of prefrontal and hippocampal time cells during the delay period, and test the stability of time cell firing field and theta phase precession slope during running at different treadmill speeds.

2 | METHODS

2.1 | Subjects

Three male Long-Evans rats (Charles River Laboratories), aged 3–12 months, weighing between 350–450 g were used for these experiments. Rats were individually housed in plexiglass cages in a temperature and humidity controlled vivarium with a 12 h light/dark cycle. During the first week of habituation and handling, animals had free access to food and water. For all subsequent behavioral training and recording sessions, animals received reduced food and water but were kept at a minimum of 85% of their ad libitum weight. All experimental procedures were performed in compliance with the guidelines of the National Institutes of Health and the Institutional Animal Care and Use Committee at Boston University.

2.2 | Behavioral training and apparatus

The task environment was a custom-built wood maze (135 L × 71 W × 90 H cm) consisting of a study arena (30 L × 30 W cm), motorized treadmill (Columbus Instruments, 40 L × 14 W cm), test arena (40 L × 40 W cm), and return arm (122 L × 7.6 W cm). In the study arena, two objects were fixed on a rotating platform and separated by a wall such that only one object was pseudorandomly presented at the start of each trial, while the other object was hidden behind the wall. The objects consisted of two polycarbonate cylinders (7 cm high with a diameter of 8 cm), filled with either purple beads scented with blueberry oil or orange yarn scented with cumin. Each object was equipped with an infrared break beam sensor (Adafruit) to precisely detect when the animal's nose crossed the mid-diameter of the cylinder, and a water port (1.5 cm diameter) was located in the center for delivering 10% sucrose water reward. An automatic door was positioned at the front of the treadmill to divide the study and test arenas, and an infrared break beam sensor (Adafruit) was positioned two inches from the front of the door on the treadmill to detect the rat's presence on the treadmill. In the test arena, the same two objects were placed on a rotating platform but without the dividing wall so that animals could choose either object. On each trial, the position of the

test objects changed pseudorandomly to either left or right. The door and object platforms were actuated by hobby servo motors, reward delivery via solenoids, which were all controlled by an Arduino Mega 2560 microcontroller. Custom MATLAB and Arduino code used for automated control of the behavioral task is available at https://github.com/winnyning/TimeCells.

At the start of all experiments, animals were acclimated to the testing room and handled by researchers for at least a week. Rats were then trained to consume Froot Loops (Kellogg's) and 10% sucrose water (Sigma-Aldrich) from the experimenters' hands. Once animals readily consumed both rewards from researchers, they were introduced to the maze apparatus to perform a delayed match to sample task.

On the first day of habituation, animals freely traversed the environment and foraged for randomly dispersed Froot Loops. On subsequent days, they were shaped to sample the objects in the study and test phase for an immediate sucrose water reward. After animals readily consumed reward from all objects, they began training on a blocked object discrimination task. In this stage, the revealed study object remained fixed and garnered a small water reward, but the animal was required to sample the pseudorandomly positioned matching test object for a larger reward. During this phase, rats were required to run in a single direction around the maze, from the study to the test arena, and then around the return arm. Rats were also shaped at this stage to remain at the rewarded objects for 2 s before reward was administered. Importantly, animals were allowed to sample either object as many times as necessary for shorter than 2 s before holding for 2 s to indicate a choice. Reward administration was accompanied by an audible click from the solenoid as the water port was activated. During an incorrect choice, no reward was given and a 261 Hz tone was played from a piezo buzzer for 0.5 s to indicate a miss.

Over the first six to eight weeks of training, animals started with large blocks (10–20 trials) of the same rule, either matching beads or yarn with no treadmill delay. Once performance levels exceeded 75% correct after 50 trials of a given block size, the block size decreased in small increments until animals were performing well at random trials in which beads or yarn was presented pseudorandomly with no delay. Subsequently, we introduced a temporal delay between the study and test phase by requiring animals to run on a treadmill at a speed of 30 cm/s to ensure spatial location, behavior and other sensory inputs remained constant across the delay. Once animals grew accustomed to the treadmill, the temporal delay gradually increased up to 8 seconds. Typically, animals took three to five months to be fully trained on the delayed match to sample task, consistently performing at over 75% correct for 60–100 trials per day.

2.3 | Stereotaxic surgery for hyperdrive implantation

Once animals reached the performance criterion (at least 75% correct trials for 4–8 s delay), rats received free food and water for a week, and then were surgically implanted with custom-built hyperdrives under aseptic conditions. Each hyperdrive contained up to 24 independently movable tetrodes, targeted unilaterally to the left hemisphere of the medial prefrontal cortex (anterior/posterior [AP] +2.5 mm, medial/lateral [ML] +0.6 mm, relative to bregma) and dorsal CA1 of the hippocampus (AP −3.6 mm, ML +2.6 mm, relative to bregma) for simultaneous electrophysiological recordings. Each tetrode was composed of four intertwined nickel-chrome wires (12 μm diameter, RO 800, Sandvik Precision Fine Tetrode Wire) and the tips were gold-plated (non-cyanide gold solution, SIFCO) to lower the final impedance to around 200 kΩ at 1 kHz (nanoZ, Neuralynx).

Anesthesia was induced via inhalation of 5% isoflurane (Henry Schein Animal Health) in oxygen. Once the animal was anesthetized, as determined by a lack of response to a toe or tail pinch, the head was shaved and the rat was transferred from an induction chamber to a stereotaxic frame (Kopf Instruments). Animals were stabilized at 1.5%–3% isoflurane for the entire duration of the surgical procedure with continuous body temperature and heart rate monitoring (PhysioSuite, Kent Scientific). Animals received preoperative injections of the analgesic buprenorphine hydrochloride (Buprenex, 0.03 mg/kg intramuscular, Reckitt Benckiser Healthcare), antibiotic cefazolin (50 mg/kg intramuscular, WG Critical Care), anti-inflammatory Rimadyl (5 mg/kg subcutaneous, Zoetis Inc.), and respiratory stabilizer atropine (0.05 mg/kg subcutaneous, Henry Schein Animal Health). After cleaning the animal's head with chlorhexidine and alcohol, a 10 mm midline incision was made and held open by hemostats or nylon sutures (Ethicon) to expose the skull. Surrounding connective tissue and fascia were cleared to reveal bregma and lambda landmarks and the skull was leveled. One to two screws were implanted above the cerebellum to serve as a ground signal, and six to eight anchoring screws were positioned around the perimeter of the skull and covered with Metabond cement (Parkell). Two large craniotomies centered around the left medial prefrontal cortex and dorsal CA1 of the hippocampus were performed. After removing the dura mater, the guide cannulae of the hyperdrive were positioned inside the two craniotomies, on the pial surface above the brain. Excess gaps between the craniotomies and cannulae were filled with vaseline and a silicone polymer Kwik-Cast (World Precision Instruments), and the hyperdrive implant was affixed to surrounding screws using dental acrylic (Perm Reline, Coltene). Once the hyperdrive implant was firmly secured, an antibiotic ointment (Neosporin) was applied and the wound was closed using absorbable Vicryl sutures (Ethicon) if needed. Finally, all tetrodes targeting the prefrontal cortex and hippocampus were gradually lowered 0.85–1.5 mm into brain tissue, prior to removal of anesthesia. For postoperative care, animals were administered with Buprenex (0.03 mg/kg intramuscular), cefazolin (50 mg/kg intramuscular), and Rimadyl (5 mg/kg subcutaneous) twice daily for two to three consecutive days following surgery. Animals were given a week for recovery with ad libitum access to food and water before starting electrophysiological recordings. During the recovery period and subsequent retraining on the delayed match to sample task, tetrodes were gradually descended into the medial prefrontal cortex and dorsal CA1 of the hippocampus, moving in increments as small as 0.02 mm (1/16 of a turn). To confirm the location of tetrodes

within CA1 of the hippocampus, we observed the presence of established electrophysiological signatures of the pyramidal layer, including multi-unit activity, strong theta in the local field potential, and sharp-wave ripple activity.

2.4 | In vivo electrophysiological recordings

All electrophysiological recordings were collected using a 96 channel Multichannel Acquisition Processor (MAP) recording system (Plexon). For single-unit activity, each channel was amplified (1,000 to 10,000x), bandpass filtered between 200 Hz to 8.8 kHz, and digitized at 40 kHz. Spiking activity was referenced to a local tetrode without clear unit activity to remove any electrical noise or movement related artifacts. Local field potentials were amplified (1,000x), bandpass filtered between 1.5 to 300 Hz, and digitized at 1 kHz. The continuous LFPs were uniformly referenced to cerebellar ground screws. Action potentials of neurons were detected via threshold crossing, which was manually set for each tetrode. Spike data were sorted from each tetrode into individual single units via manual cluster cutting using Offline Sorter (Plexon) and the following waveform parameters: peak-valley, valley, valley full width at half maximum, peak to valley ticks, energy, and principal components. Unit isolation quality was quantified using standardized L_{ratio} and isolation distance metrics (Schmitzer-Torbert et al., 2005).

Behavioral and positional data were recorded with Cineplex Studio (Plexon) using two overhead cameras, one positioned above the entire behavioral apparatus and another above the test box, sampled at 80 Hz, and were synchronized to the neural data acquisition system. The animal's position was tracked using two light-emitting diodes attached to the recording headstage. Timestamps of behavioral events were automatically strobed via transistor–transistor logic (TTL) pulses to the digital input board within the Plexon MAP system upon infrared break beam sensor crossings, door movements, and water reward deliveries.

2.5 | Behavioral testing

After a week of recovery from surgery, animals were food and water restricted again, maintaining no less than 85% of their ad libitum weight. Rats reacclimated to the testing environment and were retrained on the delayed match to sample task until performance reached above 75% correct for 60–100 trials of 8 s treadmill delay for multiple consecutive days. Once tetrodes were lowered to the desired depth and rats reached the performance criterion, recording sessions commenced.

Prior to beginning a recording session, the animal was placed on an elevated pedestal to connect to electrophysiological acquisition equipment. Each session consisted of 60–100 trials of 8 s treadmill delay. For each trial, the rat was randomly presented with one of two objects (beads or yarn) during the study phase. The animal was required to sample the object for 2 s for a small 10% sucrose water reward and then ran on an 8 s treadmill delay held at a constant speed of 30 cm/s. The start and stop of the treadmill were abrupt. The full period of both acceleration and deceleration were included within the 8 s, but these full periods were very brief intervals. After the mnemonic delay, an automatic door opened and the animal entered the test box. The animal either correctly matched the same object sampled previously by holding their nose in front of the object pot for 2 s and received a 10% sucrose water reward, or made an incorrect response (no reward). After the test phase, the animal ran along a return arm that circled back to the study phase and the next trial began. Generally, after each recording session, tetrodes were lowered to reduce the likelihood of recording from the same neurons for multiple sessions.

Rats performed two different variations of the delayed match to sample task: normal 8 s delay or 8 s delays with different treadmill speeds. For the normal 8 s sessions, each trial had a fixed treadmill delay of 8 s and the treadmill speed was held constant at 30 cm/s. For the different treadmill speed sessions, each trial had a fixed 8 s delay but the treadmill speed pseudorandomly varied (25, 30, 35, 40, and 45 cm/s).

2.6 | Histology

Upon completion of the experiments, rats were anesthetized with 5% isoflurane in oxygen. To confirm tetrode recording locations, small electrolytic lesions at the tips of the tetrodes were created by passing 40 μA of current through each wire until the connection was severed (normally 1–10 s). Animals were then administered an overdose injection of Euthasol (50 mg/kg, intraperitoneal, Virbac AH, Inc.), and were transcardially perfused with cold 0.05 M KPBS, followed by 10% phosphate buffered formalin. The implanted hyperdrive was removed and the brain was extracted from the skull and stored in 10% phosphate buffered formalin at 4°C. A week before slicing, the brains were transferred to a 30% sucrose solution in 0.05 M KPBS for cryoprotection. Immediately prior to sectioning, brains were flash-frozen (Freeze It Spray, Fisher Scientific) and sliced into 40 μm coronal sections using a cryostat (Leica CM3050S). Brain sections were mounted onto gelatin subbed microscope slides (SouthernBiotech) and subsequently stained with cresyl violet for histological confirmation of tetrode recording locations. Histological images were acquired using a Nikon Eclipse Ni-E microscope with a 4x or 10x objective lens. Tetrode lesions and tracts in the prefrontal cortex and dorsal CA1 of the hippocampus were verified and registered to turn logs and images of the hyperdrive implant guide cannulae.

2.7 | Unit quality and classification

All analyses were performed using custom code in MATLAB (MathWorks). To quantitatively evaluate cluster quality, standard L_{ratio} and isolation distance metrics were calculated from a 128 dimensional

feature space (Schmitzer-Torbert et al., 2005). Accepted clusters had an isolation distance above the 5th percentile (80.94) and L_{ratio} below the 95th percentile (0.19). Well isolated units that passed cluster quality thresholds were then classified into putative pyramidal neurons or interneurons based on the average firing rate and waveform shape. Only pyramidal cells that had a mean firing rate below 20 Hz and waveform duration greater than 0.4 ms were included in further analyses.

2.8 | Peri-event time histograms and raster plots

For single-unit analyses, peri-event time histograms (PETHs) and raster plots were generated and time-locked to the initiation of the treadmill delay. For the PETHs, the 8 s delay period was divided into 100 ms nonoverlapping bins and the trial averaged firing rate was calculated and then smoothed with a Gaussian kernel with a standard deviation of 200 ms. For all analyses, the PETHs were restricted to only the mnemonic delay, starting from when the animal crossed the infrared break beam sensor causing the treadmill to start, to when the treadmill stopped moving and the door to the test box automatically opened.

2.9 | Identification and characterization of temporally modulated cells

To quantify the temporal firing field properties of individual neurons, we calculated sparsity, temporal information (bits per spike), and peak firing rate for each unit from the PETH as described above. Sparsity was computed using the following equation (adapted from Skaggs et al., 1996):

$$\text{Sparsity} = 1 - \frac{(\sum p_i \lambda_i)^2}{\sum p_i (\lambda_i)^2}$$

where i is the temporal bin number, p_i is the occupancy probability of time bin i, and λ_i is the mean firing rate of the cell at time bin i.

Sparsity values ranged between 0 and 1, where a value closer to 0 indicates a broader tuning curve, meaning that the cell is active for a larger proportion of the delay. A larger sparsity value closer to 1 indicates a narrower firing field.

Temporal information (bits per spike) quantifies the amount of information each spike conveys about time during the delay and was calculated using the following formula (Skaggs et al., 1993, 1996):

$$\text{Information} = \sum_{i=1}^{N} p_i \frac{\lambda_i}{\lambda} \log_2 \frac{\lambda_i}{\lambda}$$

where i is the temporal bin number, p_i is the occupancy probability of time bin i, λ_i is the mean firing rate of the cell at time bin i, and λ is the overall mean firing rate of the cell across all bins.

To determine significance, we performed a bootstrap permutation procedure whereby the unit's spike train for each trial was circularly shifted by a random time between 0.5 s and 7.5 s, and the mean curve was calculated 1000 times. A null distribution of shuffled scores was generated and p values were calculated via normalized likelihood. Cells were identified as temporally modulated if the likelihood of both the temporal information score and the peak firing rate were less than 0.01.

2.10 | Autocorrelogram and theta index

To calculate theta power in each unit's spike time autocorrelogram, a model was fit using a previously published method (Royer et al., 2010). First, a cell's autocorrelogram was calculated by binning spikes into 10 ms time bins, then calculating the autocorrelation at 0 to 700 ms lags (t), and scaling the maximum value to 1. The following equation was fit to the correlation values across time lags using the function fit (MATLAB):

$$y(t) = [a(\sin(2\pi\omega t) + 1) + b] * e^{\frac{-|t|}{\tau_1}} + c * e^{\frac{-t^2}{\tau_2^2}}$$

The parameter bounds were as follows: $-1 < a < 1$, $5 < \omega < 14$ Hz, $-1 < b < 1$, $-1 < c < 1$, $100\,\text{ms} < \tau_1 < 1000\,\text{ms}$, $10\,\text{ms} < \tau_2 < 100\,\text{ms}$, and the initial point began with the midpoint between each bound. The theta index was calculated as the ratio of a/b.

2.11 | Theta phase estimation

The local field potential signal of the tetrode with the most hippocampal units during the recording session was used as the LFP reference for all units on that day. The LFP signal was bandpass filtered in the theta frequency range (5 to 12 Hz) using a three-pole Butterworth filter, and the Hilbert transform was applied to obtain the instantaneous theta phase and amplitude. To prevent the overestimation of phase preferring units due to the asymmetric shape of the theta rhythm in the LFP, we adopted a previously used method of linearly interpolating phases between the peaks and troughs of the analytic signal (Belluscio et al., 2012). The LFP data were sampled at 1000 Hz and the phase of each spike was interpolated using a nearest-neighbor approach. Zero phase is defined as the peak of the theta oscillation in CA1 of the dorsal hippocampus. For each neuron, the mean theta phase was calculated using the circ_mean function in the circular statistics toolbox (Berens, 2009). Because the distribution of the mean theta phase appeared to be bimodal, we opted to use the Omnibus test, also known as the Hodges–Ajne test (Zar, 1999), for circular uniformity to identify significant phase-locking cells ($p < .05$) using the circ_otest function (Berens, 2009). This is a better alternative to the commonly used Rayleigh test as it does not make specific assumptions about the distribution, whereas the Rayleigh test is more suitable for unimodal data (Fisher, 1995). Grouping of preferred phase across cells

was tested with Rao's spacing test for circular uniformity (Batschelet, 1981) using the function circ_raotest (Berens, 2009).

2.12 | Theta phase precession

To quantify theta phase precession, we adopted a circular–linear correlation methodology similar to previously published approaches (Kempter et al., 2012; Robinson et al., 2017). Briefly, the firing field of each unit was estimated as spikes falling in the values of the top 80% firing rate bins of the delay period peri-event time histogram after rescaling the mean curve to between 0 and 1. A circular–linear correlation was fit between time x_j and spike theta phase ϕ_j using the following equation:

$$R = \sqrt{\left[\frac{1}{n}\sum_{j=1}^{n}\cos(\phi_j - 2\pi a x_j)\right]^2 + \left[\frac{1}{n}\sum_{j=1}^{n}\sin(\phi_j - 2\pi a x_j)\right]^2}$$

The best estimated slope (a) of the regression line was quantified by maximizing the mean resultant length (R) following an iterative search algorithm using fminsearch (MATLAB).

2.13 | Population vector correlation

First, a firing rate vector for each temporally modulated cell was calculated separately for even and odd trials in the same manner as used in the peri-event time histograms, but without convolving with a Gaussian kernel. Then, mean even and odd trial rate vectors were concatenated across units and all sessions. From these two 80 time bin by n unit matrices, a Spearman correlation was calculated between each column of the even trial matrix to each column of the odd trial matrix. To match unit counts across regions and to jackknife a mean correlation value, we randomly selected 128 units from each region for 500 iterations and computed the average of the resulting correlation matrices. Finally, the raw values of the HPC matrix were subtracted from those in the PFC unit matrix to yield Figure 4b.

2.14 | Bayesian decoding of time

To calculate the Bayesian posterior probability of time given the ensemble activity, a 10-fold cross-validated Bayesian decoder was used with a Poisson distribution link function. Trial rate curves were concatenated across sessions by using only the first 60 trials of every session, and the decoder was bootstrapped 500 times using 128 units randomly selected from each region. We only included temporally modulated cells in this analysis, to be consistent with the above correlation analyses. The mean posterior probability of each time given each time ensemble was calculated (Figure 4c-i, c-ii). The mean error of the decoded time across the six decoders was calculated, producing 500 error values across boots, and those values contributed to the histograms illustrated in Figure 4d,e.

2.15 | Time versus distance analyses

For the different treadmill speed sessions, peri-event time histograms and raster plots of individual units were calculated using a similar method as the constant treadmill speed sessions. For PETHs and rasters plotted as a function of time, spike timestamps were locked to the treadmill start and the 8 s delay was divided into 100 ms nonoverlapping bins. For each treadmill speed, the trial averaged firing rate was calculated and then smoothed with a Gaussian kernel with a standard deviation of 200 ms. For PETHs and rasters plotted as a function of distance, spike timestamps locked to the treadmill start were first multiplied by the treadmill speed on that trial, and then binned into 80 distance bins along with the distance of the fastest run. Then, the mean firing rate curve for each treadmill speed was calculated before registering those curves by distance, and averaging across trials for each treadmill speed.

For each treadmill speed condition (25, 30, 35, 40, and 45 cm/s), theta phase precession slopes over time and distance were calculated for each unit using a circular–linear correlation method as previously described, based on firing fields that were in the top 80% of the peak firing rate. To compare precession slopes across different treadmill speeds for each cell, values were normalized to slopes in the 35 cm/s condition.

2.16 | Generalized linear model

A generalized linear model (GLM) framework was used to analyze the relative contributions of time and distance on cell activity during the treadmill delay (Kraus et al., 2013, 2015; MacDonald et al., 2011). First, the firing of each cell was converted to spike counts for each 100 ms bin following the treadmill onset. An equivalent number of spatial bins were generated for the fastest treadmill speed, and each temporal bin was assigned to a distance bin based on the spatial bin in which the center of that time bin fell. For slower running speeds, multiple temporal bins were assigned to the same distance bin to account for the longer time duration the rat spent at that distance bin. This allowed for the calculation of the empirical mean rate curve across time and distance separately across running speeds. A GLM was then generated with the empirical time and distance firing rate curves in 100 ms bins as the predictors and then compared to that with only one of the curves as a predictor. Importantly, these two rate curves contained an equivalent number of bins (and therefore predictors) allowing for a direct comparison of the two predictor sets. To compare the likelihood of a time code over a distance code, a logistic regression model was generated to predict the likelihood of a spike at each bin on each trial given the mean firing rate curves for distance and time and the deviances of those models were compared.

3 | RESULTS

3.1 | Rats performed a delayed match to sample task with an 8 second treadmill delay

To investigate how the prefrontal cortex and hippocampus support the temporal organization of memory, we recorded 547 neurons

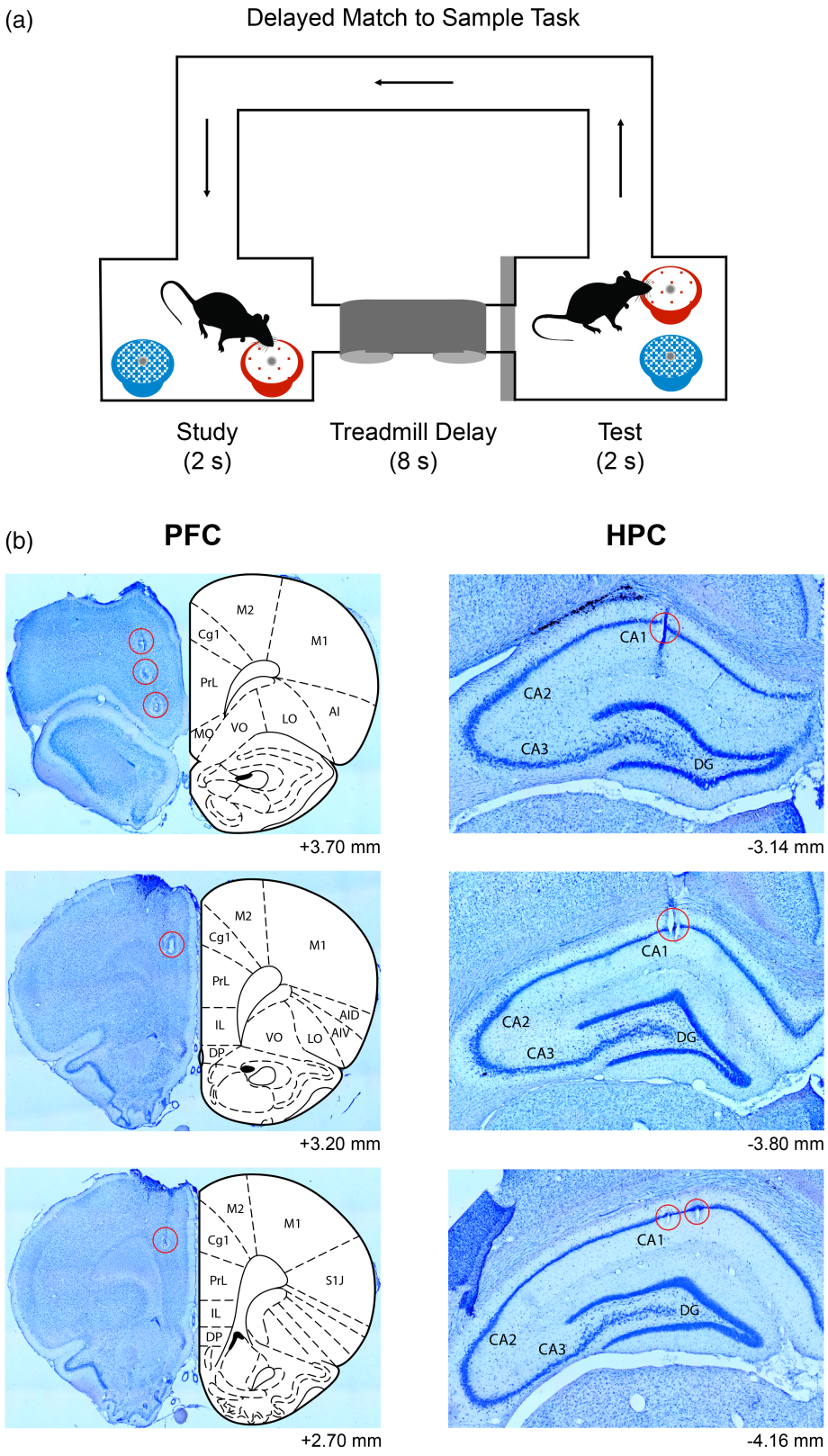

FIGURE 1 Experimental task design and tetrode recording sites. (a) Schematic of the automated delayed match to sample behavioral paradigm. Rats were presented with one of two objects, ran on a motorized treadmill for an 8 second delay held at a constant speed of 30 cm/s, and were subsequently required to select the matching object to retrieve a sucrose water reward (gray circles). (b) Recording locations of tetrodes in the prefrontal cortex (PFC), including anterior cingulate cortex (Cg1), prelimbic (PrL), and infralimbic (IL), and dorsal CA1 of the hippocampus (HPC) in representative coronal sections stained with cresyl violet. Circles indicate the final lesion marks at the most ventral positions. Schematic diagram adapted from Paxinos and Watson (1998).

extracellularly in the medial prefrontal cortex (including anterior cingulate cortex, prelimbic and infralimbic regions) and 303 neurons in dorsal CA1 of the hippocampus from male Long-Evans rats ($n = 3$) performing a delayed match to sample task (Figure 1a). Each animal was unilaterally implanted with a dual-site hyperdrive with 24 independently movable tetrodes (96 channels) and recording locations in the prefrontal cortex and dorsal hippocampus were confirmed with histology (Figure 1b). Well isolated units were identified using standard L_{ratio} and isolation distance metrics and putative pyramidal cells with a mean firing rate below 20 Hz and waveform duration

greater than 0.4 ms were included in further analyses. On each trial, rats sampled one of two objects for 2 s, then ran on a treadmill mnemonic delay for 8 s held at a constant speed of 30 cm/s. Controlling for spatial and behavioral variables allowed us to examine neural activity as a function of elapsed time and investigate how the prefrontal cortex and hippocampus generate an internal representation of the passage of time during the delay. After the treadmill delay, animals entered the test box and were allowed to sample the two objects. The final choice was determined by holding the nose poke response in one of the two objects for at least 2 s. Sucrose water rewards were delivered for correct trials, while incorrect trials were signaled with no reward and an auditory tone. Rats were pretrained to run 60–100

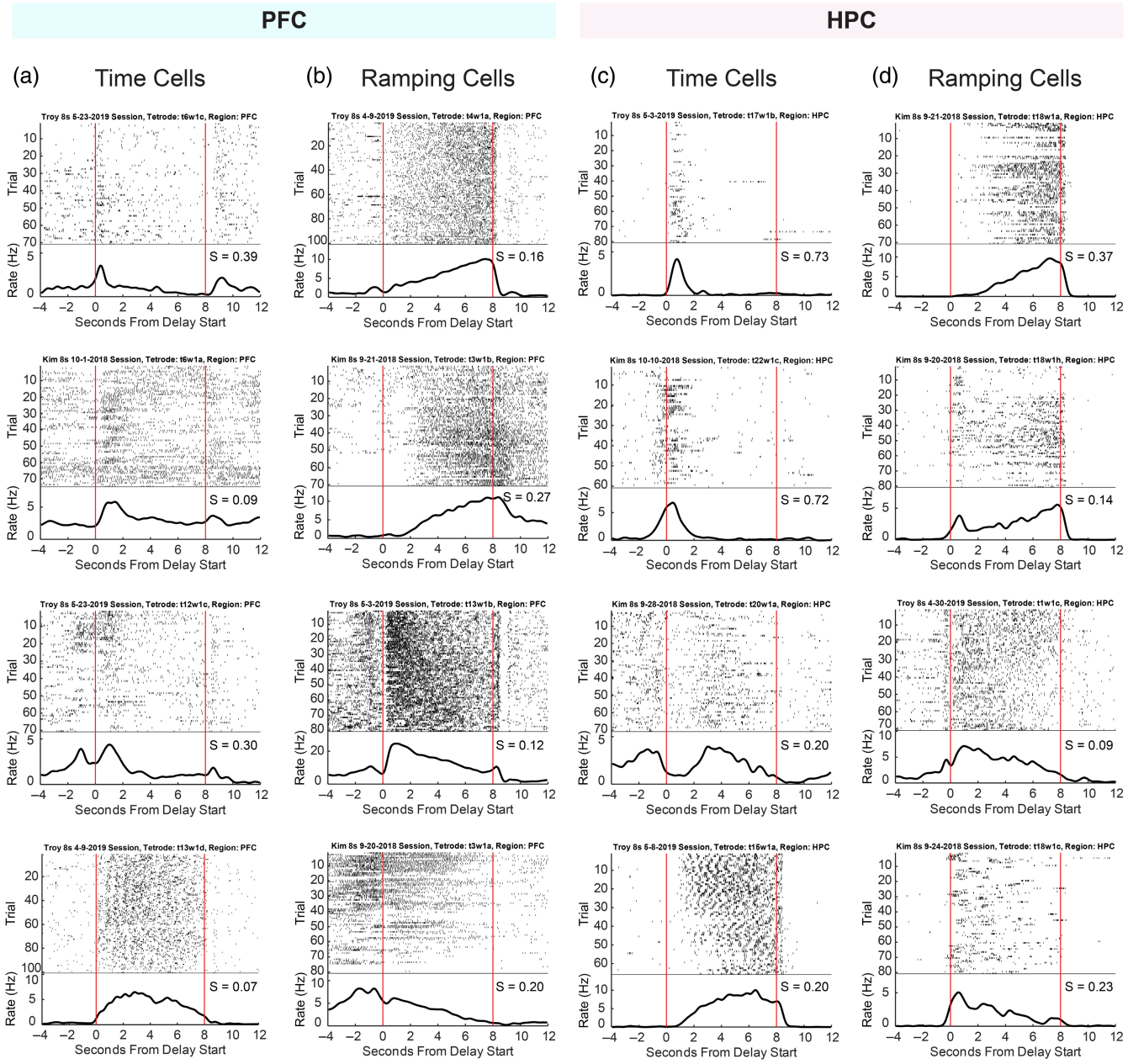

FIGURE 2 Single cells in the prefrontal cortex and hippocampus exhibit temporally modulated activity during the treadmill delay. (a–b) Examples of individual time cells and ramping cells in PFC and (c-d) dorsal CA1 of HPC during the 8 s treadmill delay. *Top*: raster plot, each row represents one trial with spiking activity aligned to treadmill delay onset. *Bottom*: peri-event time histogram showing the smoothed average firing rate (black line) across all trials in a given recording session. Red vertical lines indicate the start and stop of the 8 s treadmill delay. Time cells in PFC (a) and HPC (c) fire sequentially at specific time points, exhibiting sparse temporal firing fields that tiled the entire delay period. Some units in PFC (b) and HPC (d) were more broadly tuned, showing gradual changes in firing rate activity, either ramping up or down over the mnemonic delay. Sparsity (S) values for temporal firing fields are indicated for each cell.

trials each day, performing over 75% correct trials. Once animals reached the behavioral criteria, recording sessions began. A total of 24 sessions with constant treadmill speed were included (Rat 1: 11 sessions, Rat 2: 5 sessions, Rat 3: 8 sessions). The average performance was 83.11% ± 1.59% correct and the mean number of trials per session was 74.29 ± 1.59.

3.2 | Single neurons in the prefrontal cortex and hippocampus exhibit temporally modulated activity during the treadmill delay

We first examined the 8 second treadmill delay period to investigate how individual neurons in the prefrontal cortex and hippocampus encode temporal information to bridge the gap between discontiguous events. Recent studies have identified sequences of time cells with punctate firing fields in CA1 (Kraus et al., 2013; MacDonald et al., 2011, 2013; Mau et al., 2018; Modi et al., 2014; Pastalkova et al., 2008; Shimbo et al., 2021; Taxidis et al., 2020), CA3 (Salz et al., 2016), medial entorhinal cortex (Kraus et al., 2015), striatum (Akhlaghpour et al., 2016; Bakhurin et al., 2017; Mello et al., 2015), and prefrontal cortex (Bakhurin et al., 2017; Cruzado et al., 2020; Pilkiw & Takehara-Nishiuchi, 2018; Tiganj et al., 2017). In contrast, other studies report cells with monotonically changing firing rates in the hippocampus (Deadwyler & Hampson, 2004), prefrontal cortex (Kim et al., 2013), lateral entorhinal cortex (Tsao et al., 2018), and ventral striatum (van der Meer & Redish, 2011), either gradually ramping up or down over time, suggesting that the encoding of time could be reflected through the firing rates of individual neurons. These two complementary representations of time may support active maintenance of information during delays important for memory encoding.

To assess single-unit activity in the prefrontal cortex and dorsal CA1 of the hippocampus, rasters and peri-event time histograms centered around the onset of the treadmill delay were compared (Figure 2). Consistent with previous reports, many hippocampal time cells exhibited sparse rate curves, firing only at specific time points that tiled the entire mnemonic delay (Figures 2c and 3a). We also observed hippocampal cells with less punctate activity that slowly ramped up or down during the delay (Figure 2d), similar to the delay cells reported in the subiculum and CA1 during a spatial delayed nonmatch-to-sample task (Deadwyler & Hampson, 2004; Hampson & Deadwyler, 2003). In the prefrontal cortex, some units exhibited responses similar to time cell activity in CA1 with discrete temporal firing fields, firing sequentially at specific moments in time (Figure 2a). Strikingly, a majority of prefrontal units exhibited ramping up or decaying activity (Figure 2b), similar to cells previously reported in rat prefrontal cortex (Kim et al., 2013; Tiganj et al., 2017), lateral entorhinal cortex (Tsao et al., 2018), monkey entorhinal cortex (Bright et al., 2020), and human entorhinal cortex (Umbach et al., 2020).

To identify cells significantly modulated by delay time regardless of the firing rate curve shape, we set a criteria of information score exceeding $p < .01$ and peak firing rate exceeding $p < .01$

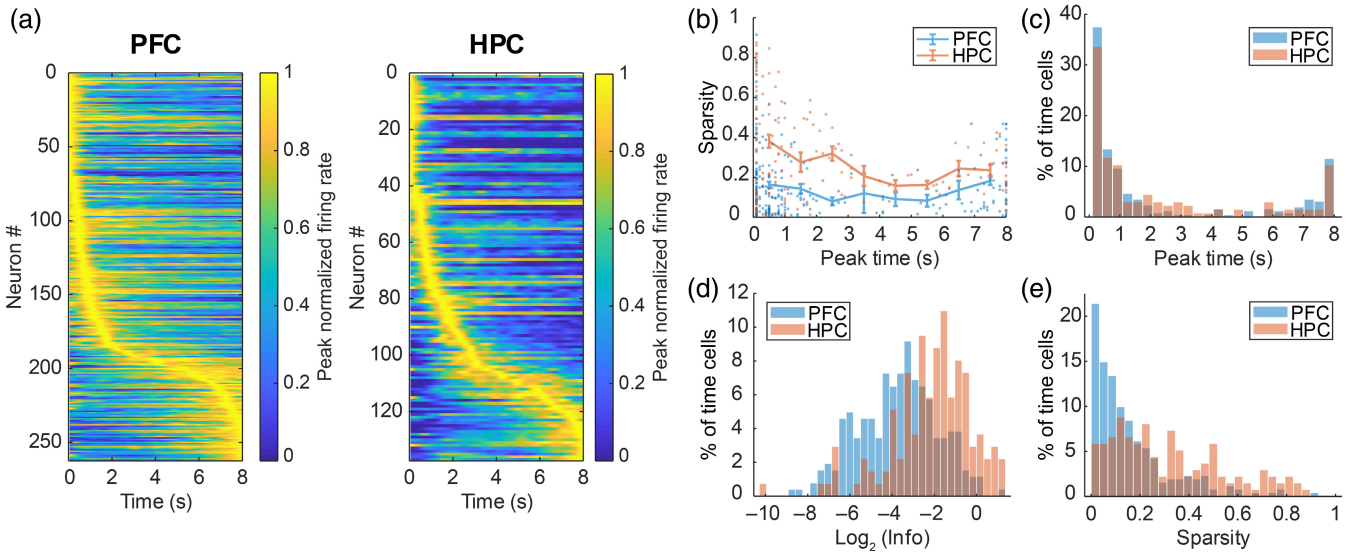

FIGURE 3 Sequential population activity spans the entire delay with hippocampal neurons showing sparser temporal firing fields than prefrontal cells. (a) Ensemble firing patterns of temporally modulated cells in PFC (left) and HPC (right) during the 8 s treadmill delay across all animals. Each row depicts the peak normalized firing rate of one neuron, sorted by the peak firing time. Yellow indicates high firing rate, while blue corresponds to low firing rate. (b) Sparsity of firing fields as a function of peak firing time. Each dot represents a temporally modulated cell in PFC (blue) or HPC (red) and lines indicate the mean sparsity ± SEM at each time bin during the delay. (c) Histogram of peak times of temporal firing fields in PFC and HPC. (d) Distribution of temporal information scores (bits per spike) for cells in PFC and HPC. (e) Histogram showing the distribution of sparsity values of all temporally modulated cells in PFC and HPC. High sparsity values closer to 1 indicate narrow field widths, whereas low sparsity values closer to 0 indicate broader firing fields.

when compared to a trial-wise circularly shifted spike train (greater than 99th percentile of 1000 bootstrap permutations). Around 47.9% of prefrontal cortex neurons ($n = 262/547$) and 45.2% of hippocampal neurons ($n = 137/303$) were classified as temporally modulated cells. The percentage of temporally modulated cells in the prefrontal cortex and hippocampus was not significantly different (Chi-squared test of independence, $\chi^2 = 0.20$, $p(1) = .65$).

3.3 | Sequences of hippocampal time cells exhibit sparser temporal firing fields than prefrontal cells

We then examined the ensemble activity of all identified temporally modulated cells in the prefrontal cortex and hippocampus and sorted each cell by its peak firing time. Temporal firing fields in both the prefrontal cortex and hippocampus span the entire 8 second delay (Figure 3a), with more cells firing at the beginning and end of the delay as these are behaviorally salient cues for the animals (Figure 3c). This is consistent with previous work showing a nonuniform, compressed distribution of time cells with decreasing temporal resolution over time (Howard et al., 2014; Kraus et al., 2013; Salz et al., 2016; Tiganj et al., 2017). Cells that fire early in the delay tend to be more sparse (narrow time fields), and the firing fields get broader as time progresses (Figure 3b). The slight increase in activity near the end of the 8 s interval could reflect an anticipatory response for the end of the delay and expectation of upcoming reward, similar to the increase in number of place fields concentrated near reward sites (Dombeck et al., 2010).

Based on the preceding observations, we next quantified the firing rate curve shape of time coding cells in each region by calculating sparsity and information (bits per spike) for each unit's delay firing rate curve. Sparsity and information scores have been used previously to describe time cells and place cells, capitalizing on the high clustering of spikes to one moment in time or position in space. These two metrics can capture differences in firing rate activity to distinguish punctate time cells from broad ramping activity. For temporally modulated cells, the trial averaged delay rate curves of hippocampal units were sparser (Figure 3e, PFC mean sparsity = 0.16 ± 0.01, HPC mean sparsity = 0.32 ± 0.02, Wilcoxon rank-sum test, $z = 7.43$, $p = 1.06 \times 10^{-13}$), and contained more temporal information than prefrontal cortex cells (Figure 3d, PFC mean temporal information (bits per spike) = 0.16 ± 0.02, HPC = 0.43 ± 0.04, Wilcoxon rank-sum test, $z = 7.74$, $p = 9.92 \times 10^{-15}$). Furthermore, this effect was apparent at every second throughout the whole delay (Figure 3b, Wilcoxon signed-rank test, $z = -2.52$, $p = 1.17 \times 10^{-2}$). Interestingly, hippocampal time cells fired many fewer spikes than prefrontal cells during the mnemonic delay, which may explain the differences in information rates across regions. Therefore, we conducted a complementary analysis where we used an information theory approach that considered trial-by-trial firing rates (Olypher et al., 2003). Crucially, this analysis measures the information content carried in the cells' tuning curves after considering variance across trials, and is robust to differences in spike counts. Therefore, by using "positional" information scores, we were able to determine whether the increased information observed in the smaller firing fields in the hippocampus was consistent across trials. This analysis revealed that there was neither a higher maximum information (Wilcoxon rank-sum test, $z = 9.99 \times 10^{-1}$, $p = .31$), nor a higher mean information (Wilcoxon rank-sum test, $z = 1.05$, $p = .29$) in the hippocampus, compared to the prefrontal cortex. Therefore, this result suggests that while hippocampal cells have a higher information content in the average tuning curves, a closer look suggests that this is merely due to the higher concentration of spikes in a smaller region of time.

Additionally, there was a significant difference in the mean firing rate of temporally modulated cells in the prefrontal cortex and hippocampus (PFC = 3.49 ± 0.27 Hz, HPC = 2.29 ± 0.29 Hz, Wilcoxon rank-sum test, $z = 3.92$, $p = 8.70 \times 10^{-5}$), however, no difference was observed in the peak firing rate (PFC = 5.56 ± 0.35 Hz, HPC = 4.74 ± 0.42 Hz, Wilcoxon rank-sum test, $z = 1.58$, $p = .11$).

3.4 | Bayesian decoding reveals that population activity in the hippocampus encodes time more accurately early in the delay, whereas the prefrontal cortex is more accurate later in the delay

While prefrontal cortex and hippocampal units exhibited different firing rate curve characteristics across the delay, it was unclear whether this translated into different information content about time during the delay. To address this question, we used population vector analyses to examine ensemble coding during the delay. We constructed ensemble-rate vectors from units in each region during the delay, and generated a correlation matrix by calculating the Spearman correlation of the normalized ensemble activity vectors sampled from each time bin during the delay to activity vectors sampled from every other time bin during the delay. To capture the consistency of ensemble activity, we correlated vectors averaged across even trials to those averaged across odd trials (Figure 4a-i,a-ii). Ensemble correlation matrices in both the prefrontal cortex and hippocampus appeared to code for time, showing high correlation values between ensembles sampled from similar times (close to diagonal) and low values between ensembles far in time (far from diagonal). A difference between the matrices revealed much higher correlation values in the prefrontal cortex when comparing the first 2 s of the delay to the following 2 s (two yellow areas at top left), suggesting a less precise time code in the prefrontal cortex at the onset of the delay (Figure 4b). To investigate this effect, we applied a naïve Bayesian classifier to quantify the temporal precision of delay activity in each region (Figure 4c-i,c-ii). When the whole 8 s delay was considered, differences appeared in the decoding accuracy between the prefrontal cortex and hippocampus (Figure 4d, Wilcoxon rank-sum test, $z = -12.14$, $p = 6.37 \times 10^{-34}$). As observed, the distributions of decoding error for the whole delay did not follow a unimodal distribution. For further investigation, we subdivided the

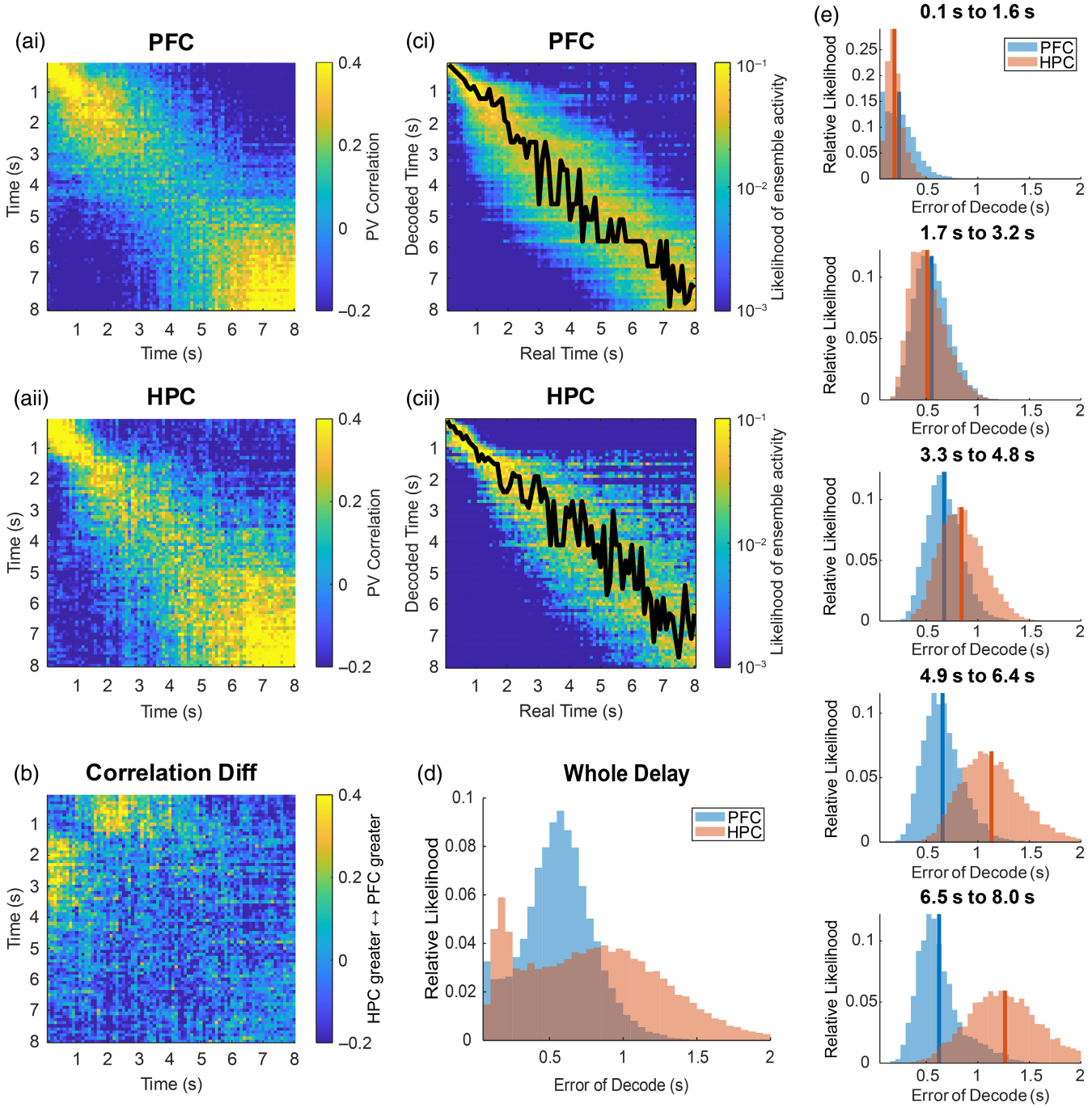

FIGURE 4 Bayesian decoding reveals that population activity in the hippocampus encodes time more accurately early in the delay, whereas the prefrontal cortex is more accurate later in the delay. (ai-aii) Cross-temporal ensemble correlation matrix for the 8 s delay. Correlation values are high between population vectors taken closer in time, especially when comparing early to early, and late to late ensemble activations. Population vectors were constructed from the mean tuning curves across the delay in 100 ms bins using 128 randomly selected cells from each region. (b) Difference in population vector correlation values between PFC and HPC. High values in yellow areas comparing early to mid-delay suggest greater PFC ensemble similarities across wider time gaps early in the delay. (ci-cii) Naïve Bayesian decoder success probability across the delay. Decoder was trained in a 10-fold manner with 128 unit ensembles at the same bin size as above. Black line indicates the most likely decoded time across decoders. (d) Histogram of decoding error across the whole 8 s delay suggests that the HPC decoder often makes either very small or very large errors, whereas the PFC decoder often makes small to moderate errors (Wilcoxon rank-sum test, $p < .001$). (e) Distribution of decoding error for delay quintiles across time. The HPC decoder is more accurate early in the delay, whereas the PFC decoder is more accurate later in the delay. The HPC decoder error was significantly smaller from 0.1 to 1.6 s and 1.7 to 3.2 s, and larger from 3.3 to 4.8 s, 4.9 to 6.4 s, and 6.5 to 8.0 s, compared to PFC (Wilcoxon rank-sum test, $p < .001$ for all quintiles).

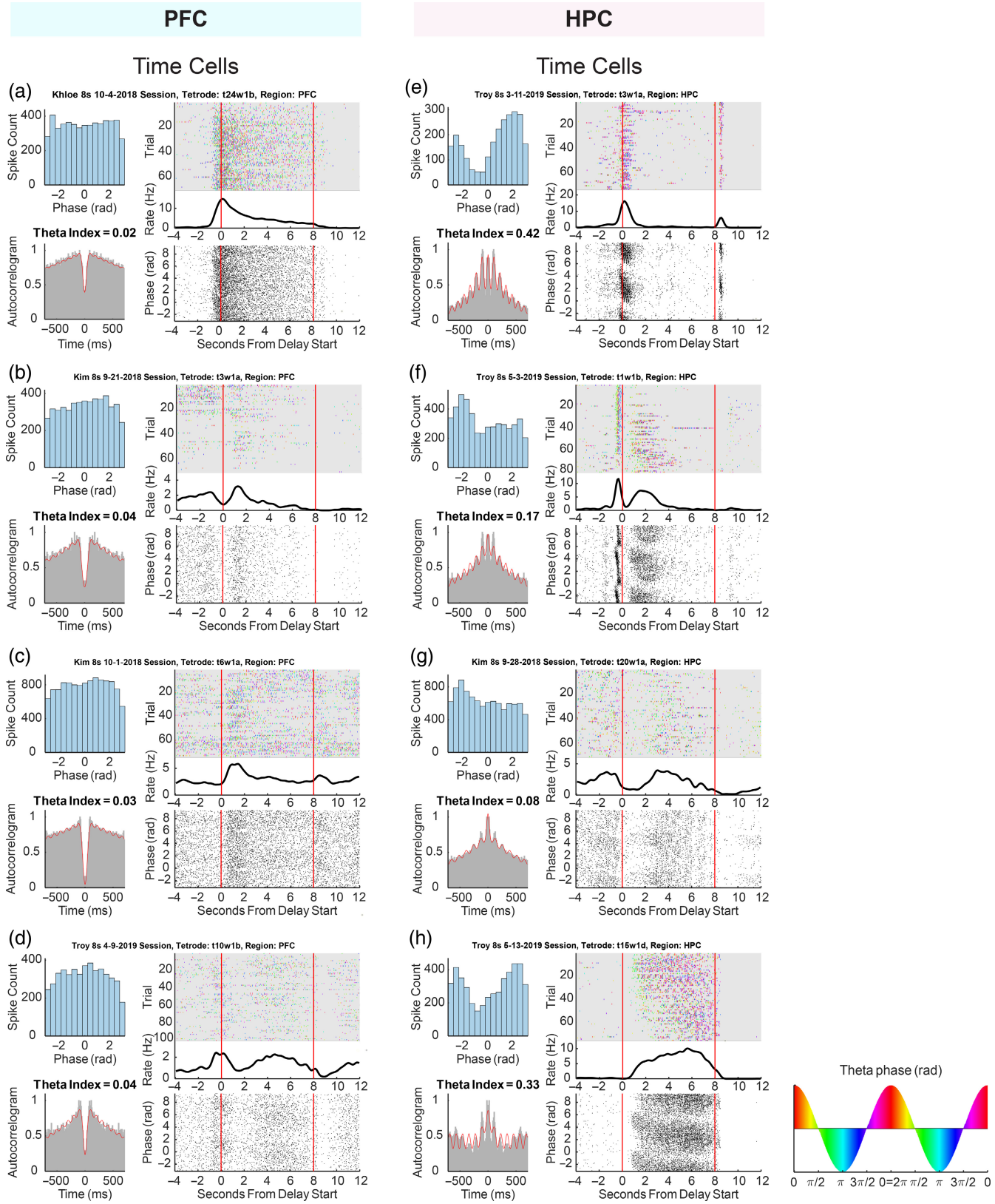

FIGURE 5 Time cells in the prefrontal cortex and hippocampus exhibit theta phase precession. (a–h) Rasters, peri-event time histograms, theta phase-time plots, phase histograms, and autocorrelograms of four example neurons in each region. *Top right*: raster plot of spikes, color-coded by theta phase. *Middle right*: peri-event time histogram showing the mean firing rate (black line). *Bottom right*: theta phase plot depicting spiking activity plotted as a function of theta phase and delay time. Two theta cycles are displayed for clarity. Red vertical lines indicate the start and stop of the 8 s treadmill delay. *Top left*: Histogram of theta phase for all spikes for each cell. *Bottom left*: spike time autocorrelogram showing the intrinsic theta rhythmicity of each neuron and the fitted model (red line) used to calculate the theta index, a measure of the strength of theta modulation. (a–d) PFC time cells show less phase specificity and weaker theta phase precession. (e–h) Hippocampal CA1 time cells with sparse firing fields show steeper theta phase precession and stronger theta rhythmicity.

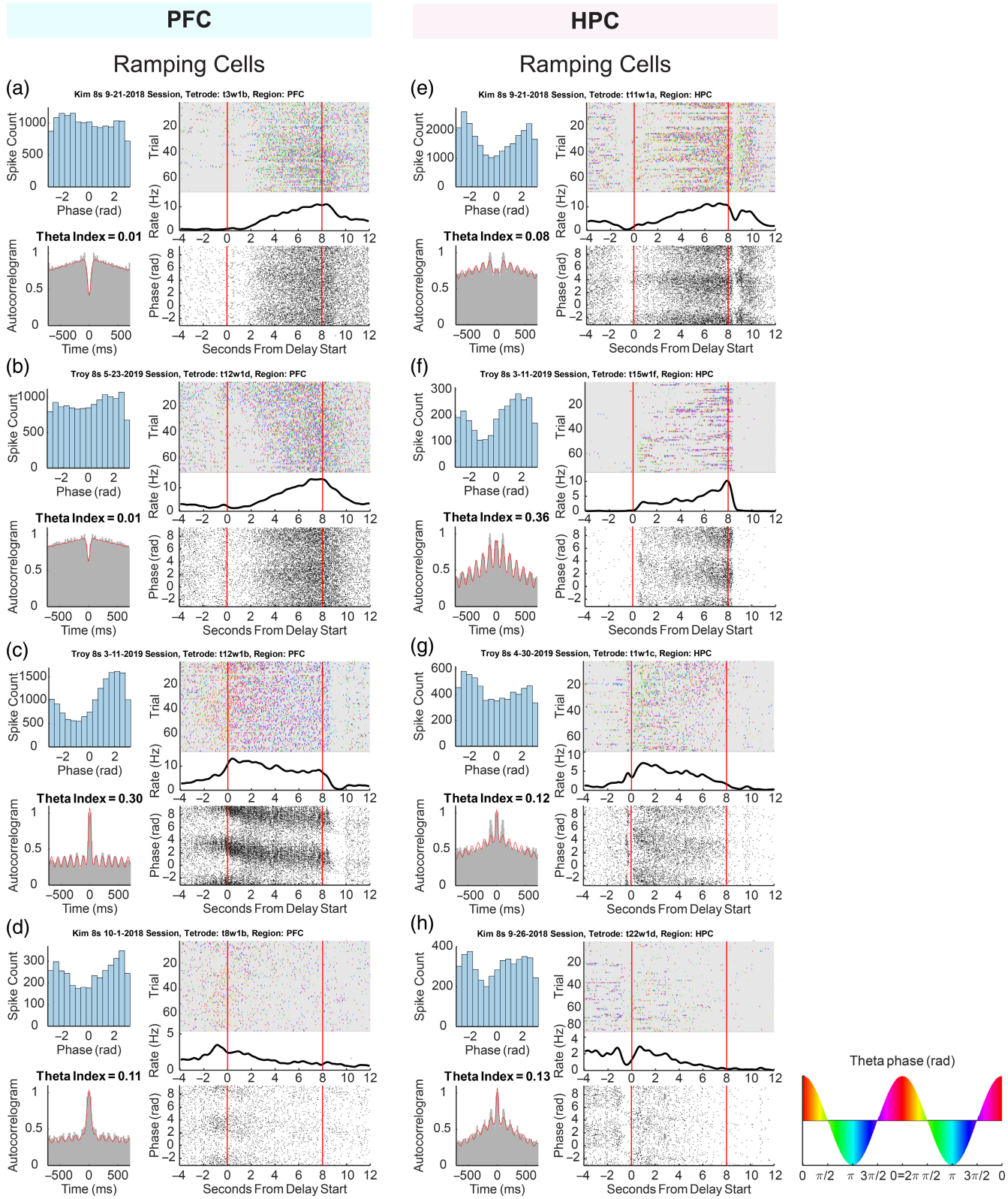

FIGURE 6 Temporally modulated cells with monotonically changing firing rates in the prefrontal cortex and hippocampus show shallow theta phase precession slopes. (a–h) Rasters, peri-event time histograms, theta phase-time plots, phase histograms, and autocorrelograms of four example neurons in each region. *Top right*: raster plot of spikes, color-coded by theta phase. *Middle right*: peri-event time histogram showing the mean firing rate (black line). *Bottom right*: theta phase plot depicting spiking activity plotted as a function of theta phase and delay time. Two theta cycles are displayed for clarity. Red vertical lines indicate the start and stop of the 8 s treadmill delay. *Top left*: Histogram of theta phase for all spikes for each cell. *Bottom left*: spike time autocorrelogram showing the intrinsic theta rhythmicity of each neuron and the fitted model (red line) used to calculate the theta index, a measure of the strength of theta modulation. (a,b) PFC cells with broad ramping or (c,d) decaying activity exhibit slow shifts in theta phase during the entire delay. (e,f) Hippocampal CA1 cells with ramping or (g,h) decaying activity show stronger theta rhythmicity and were associated with similar slow shifts in theta phase across the delay.

delay period into five even quintiles (Figure 4e, Wilcoxon rank-sum test, 0.1–1.6 s: $z = 14.7$; 1.7–3.2 s: $z = 17.5$; 3.3–4.8 s: $z = -50.4$; 4.9–6.4 s: $z = -91.5$; 6.5–8.0 s: $z = -95.8$, $p < .001$ for all quintiles). Importantly, the hippocampus showed a more precise time code early in the delay (first two quintiles), whereas the prefrontal cortex exhibited a more precise time code later in the delay (last three quintiles).

3.5 | Temporally modulated cells exhibit theta phase precession

We next examined the relationship between the timing of spiking activity relative to the phase of hippocampal theta oscillation. Place cells in the hippocampus and grid cells in the medial entorhinal cortex have been known to exhibit robust theta phase precession, whereby spikes fire at progressively earlier phases of theta as an animal traverses through a firing field (Jeewajee et al., 2013; O'Keefe & Recce, 1993; Skaggs et al., 1996). Phase precession is a temporal coding mechanism that allows for the compression of spatiotemporal sequences, integrating past, present, and future information within a single theta cycle, on a fast timescale required for synaptic plasticity. While a multitude of studies have documented the role of hippocampal phase precession within the spatial domain, only a few studies have observed transient phase precession in hippocampal neurons during nonspatial tasks (Takahashi et al., 2014; Terada et al., 2017; Umbach et al., 2020) and in time cells as animals are running in place

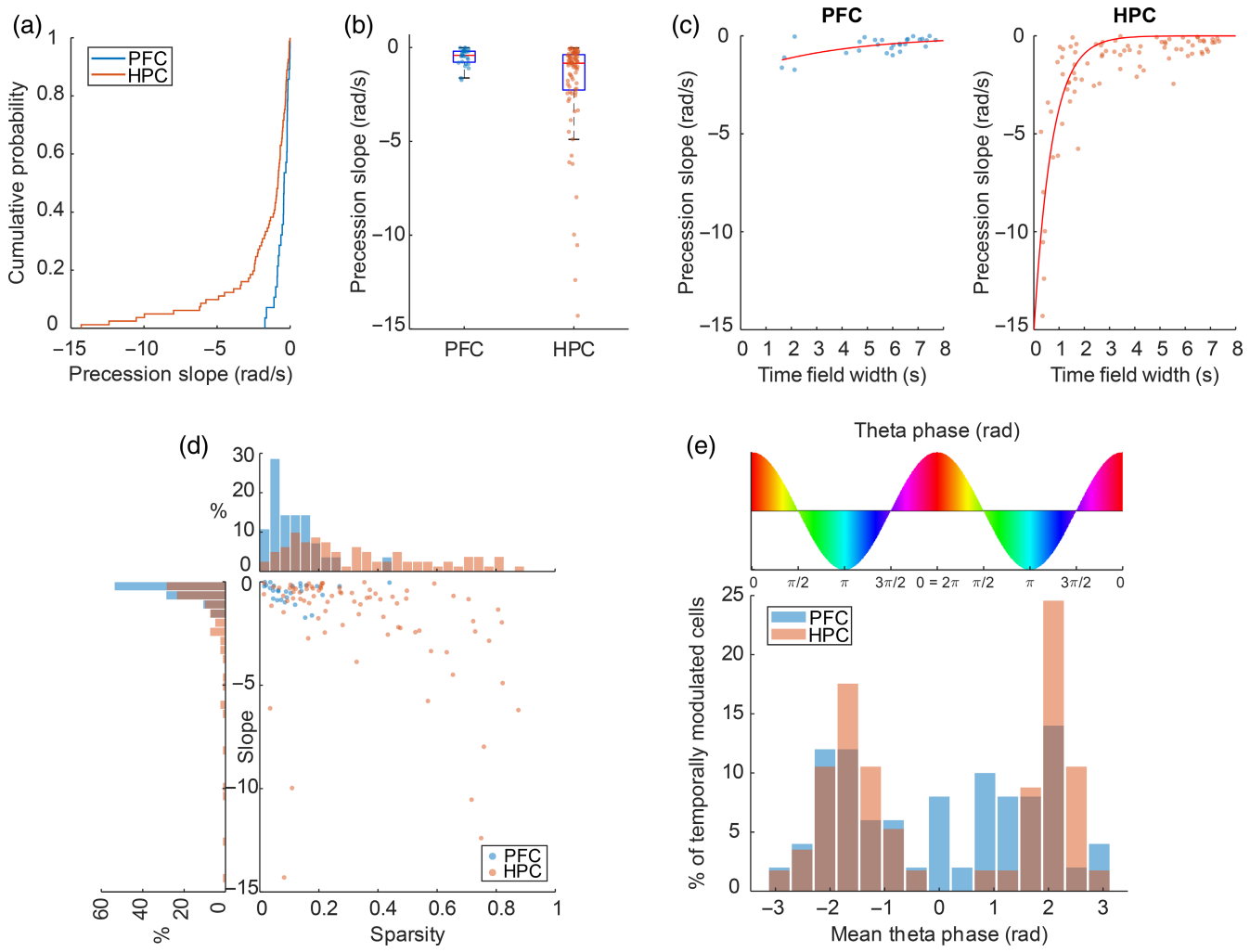

FIGURE 7 Sparse time cells in the hippocampus exhibit steeper theta phase precession slopes compared to prefrontal cortex cells. (a) Cumulative distribution of precession slopes (rad/s) for temporally modulated cells in PFC (blue) and HPC (red) exhibiting significant theta phase precession ($p < .05$). (b) Box plot of theta phase precession slopes in PFC and HPC depicting the quartiles and median slopes (red line, PFC = −0.41 rad/s, HPC = −0.84 rad/s), with a scatter plot showing individual cells (Wilcoxon rank-sum test, $p = 3.69 \times 10^{-4}$). (c) Relationship between theta phase precession slope and temporal field size for cells in PFC ($R^2 = .40$) and HPC ($R^2 = .69$). (d) Scatter plot of precession slopes (rad/s) and sparsity for temporally modulated cells with significant phase precession ($p < .05$). *Top*: Histogram of sparsity values for PFC and HPC cells. *Left*: Histogram of precession slopes (rad/s). (e) Distribution of mean theta phase for all phase-locking time cells (Omnibus test, $p < .05$).

(Pastalkova et al., 2008; Shimbo et al., 2021). Theta phase precession of temporally modulated cells during a controlled treadmill task and the role of phase precession in the prefrontal cortex have not been well characterized. To investigate whether temporally modulated cells would encode for time through the delay using theta phase, we observed the spiking activity of each neuron during the 8 s delay with respect to the phase of hippocampal theta oscillation and compared rasters, peri-event time histograms, theta phase precession plots,

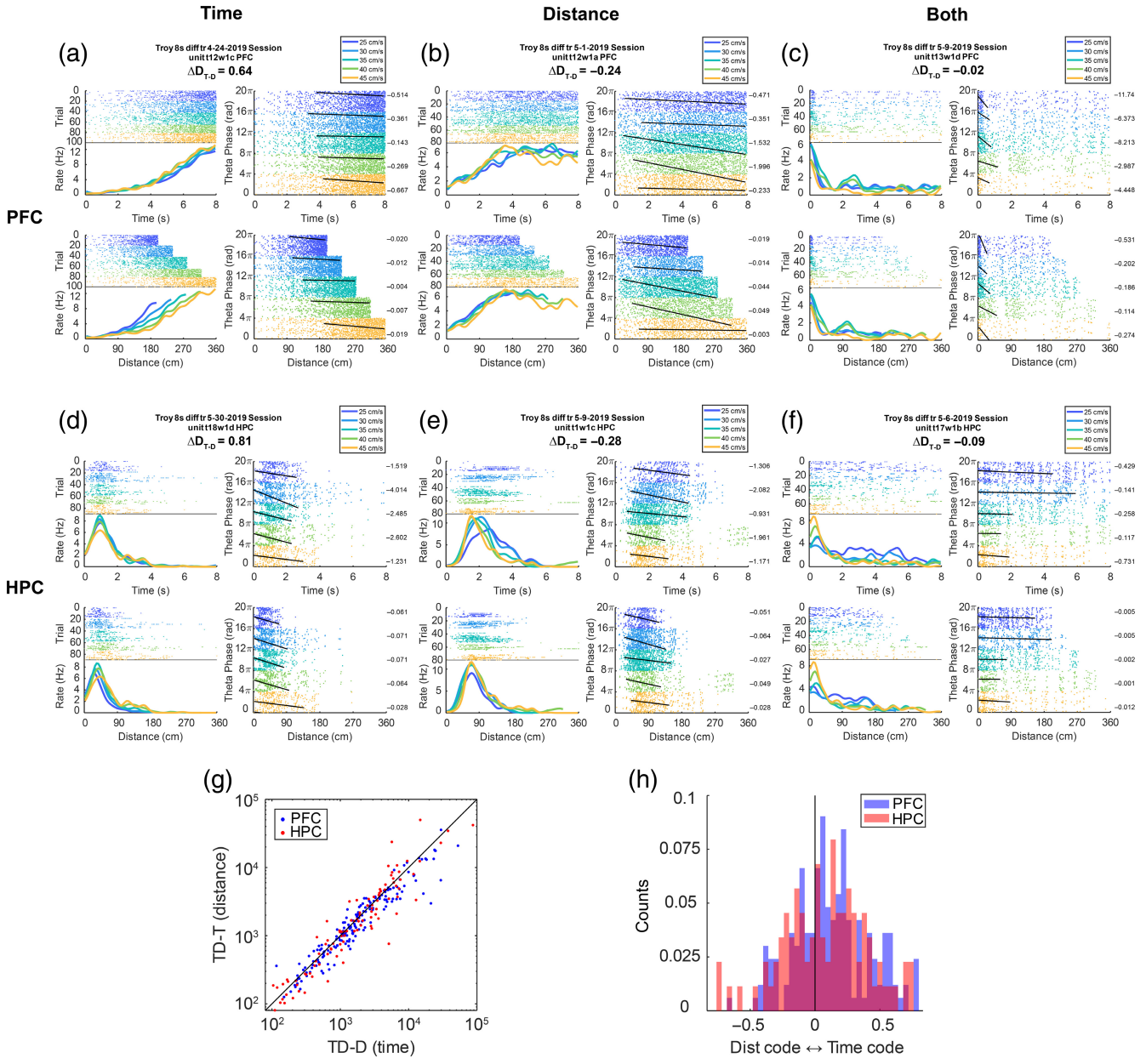

FIGURE 8 Neurons in the prefrontal cortex and hippocampus are more influenced by time than distance. (a–f) Firing patterns of individual neurons plotted as a function of elapsed time (top) or distance traveled (bottom), sorted by treadmill speed (25, 30, 35, 40, and 45 cm/s). *Left*: raster plot, each row represents one trial with spiking activity aligned to the treadmill delay onset. The slowest speed (25 cm/s) is shown on top in navy and the fastest speed (45 cm/s) is at the bottom in yellow. Below the raster is the peri-event time histogram showing the trial-averaged firing rate for each treadmill speed. *Right*: theta phase plot depicting spiking activity plotted as a function of theta phase and delay time. Two theta cycles are displayed for clarity and the circular–linear regression line (black line) used to quantify theta phase precession slope (rad/s) is indicated for each treadmill speed. Example neurons in each region showing strong tuning to time (a, d), distance (b, e), or both dimensions (c, f). Deviance (ΔD_{T-D}) values are indicated for each cell with more positive values showing a stronger influence of time, while negative values indicate a stronger influence of distance on spiking activity. (g) Scatter plot of the deviance values of each predictor to compare the influence of time or distance on spiking activity in PFC (blue) and HPC (red). Dots along the black diagonal indicate neurons with equal contribution of time and distance. (h) Histogram of g showing the distribution of time versus distance coding in each region (Wilcoxon signed-rank test, PFC: $p = 2.17 \times 10^{-7}$, HPC: $p = 1.68 \times 10^{-2}$). More positive values represent cells more influenced by time, and negative values indicate cells with larger contributions from distance information. Black line at zero represents equal contribution of time and distance.

phase histograms, and spike time autocorrelograms (Figures 5 and 6). All analyses were done with reference to hippocampal theta oscillation. Temporally modulated cells in the prefrontal cortex showed less phase specificity (Figure 5a–d) and some cells with ramping (Figure 6a,b) or decaying activity (Figure 6c,d) exhibited slow shifts in theta phase across the whole delay. This is similar to the slower rates of phase precession observed in anticipatory ramping cells recorded in the ventral striatum when animals approached an upcoming reward (van der Meer & Redish, 2011). In comparison, many hippocampal time cells with sparse firing fields exhibited steep phase precession slopes (Figure 5e–h), while some ramping (Figure 6e,f) or decaying cells (Figure 6g,h) showed slower phase precession during the entire delay. These results suggest that there may be two different time scales of theta phase precession.

3.6 | Sparse hippocampal time cells show steeper theta phase precession slopes compared to prefrontal cortex neurons

Using a circular–linear correlation method, we next quantified the slopes of theta phase precession (rad/s) for temporal firing fields, which were defined as the top 80% of a cell's peak firing rate (Kempter et al., 2012; Kraus et al., 2013; Tingley et al., 2018). A greater proportion of temporally modulated cells in the hippocampus (81/137 = 59.12%) exhibited significant theta phase precession ($p < .05$), as compared to prefrontal cells (28/257 = 10.89%). When considering only temporally modulated cells with significant phase precession (Figure 7a–d), hippocampal time cells showed steeper precession slopes, while slopes were more shallow for prefrontal units (Figure 7a,b, Wilcoxon rank-sum test, $z = 3.56$, $p = 3.69 \times 10^{-4}$). Hippocampal cells exhibited sparser temporal firing fields (HPC mean sparsity = 0.34 ± 0.03), along with steeper theta phase precession slopes (HPC mean slope = −1.94 ± 0.31, Figure 7d). For the prefrontal cortex, precession slopes were significantly more shallow (PFC mean slope = −0.50 ± 0.09) with the presence of broad, ramping activity (PFC mean sparsity = 0.11 ± 0.02, Figure 7d). These results differ from previous work where overall spatial theta phase precession occurred at a similar rate in both CA1 and PFC in a continuous spatial alternation memory task (Jones & Wilson, 2005a).

Given our finding that hippocampal units showed steeper theta phase precession slopes than prefrontal cells, we next examined whether precession slope was correlated with the temporal field size, similar to the increase in place field size and scaling of phase precession from dorsal to ventral hippocampus in the spatial domain (Jung et al., 1994; Kjelstrup et al., 2008). Using a logarithmic regression model, we observed a strong inverse relationship between precession slope and time field width for cells in the dorsal hippocampus ($R^2 = .69$) and prefrontal cortex ($R^2 = .40$, Figure 7c). Similar to place fields, an increase in time field width (length in time) was correlated with decreasing slope of theta phase precession (Figure 7c), consistent with previous studies showing that the phase shift is a function of the firing field size (Dragoi & Buzsáki, 2006; Huxter et al., 2003; Pastalkova et al., 2008). The logarithmic relationship is more evident in the hippocampus due to a greater number of sparse time fields that are smaller than 1.6 s, compared to the prefrontal cortex where broad ramping activity is more prevalent.

When considering only theta phase-locking time cells (Omnibus test, $p < .05$, PFC 50, HPC 57 cells), the theta phase distribution of hippocampal cells significantly deviated from a circular uniform distribution (Rao test, U[57] = 180.82, $p = .001$), instead showing a bimodal distribution (Figure 7e). The preferred theta phase of prefrontal cells was weakly nonuniformly distributed (Rao test, U[50] = 152.60, $p = .05$).

3.7 | Time and distance coding in the prefrontal cortex and hippocampus

Next, to disentangle the effects of spatial location, time, and distance on neural firing activity, we systematically varied the treadmill speed to regress out if neurons are tracking elapsed time or distance traveled (number of steps) during the mnemonic delay. Within a given recording session, each trial had a fixed 8 s treadmill delay but with a random speed, ranging from 25, 30, 35, 40, and 45 cm/s. We recorded a total of 13 sessions with different treadmill speeds with an average performance of 80.65% ± 2.32% and the mean number of trials per session was 82.15 ± 4.50.

From the different treadmill speed recordings, 54% of cells in the prefrontal cortex ($n = 171/315$) and 47% of cells in dorsal CA1 of the hippocampus ($n = 99/209$) were temporally modulated. We first examined single-unit firing activity during the 8 s delay period, sorted by the five different treadmill speeds from slowest (25 cm/s) to fastest (45 cm/s), and plotted activity either as a function of elapsed time or distance traveled. Cells that more reliably encode for time show the same temporal firing field regardless of running speed (Figure 8a, d, top row). When these same units were plotted as a function of distance (Figure 8a,d, bottom row), the tuning curves shifted to the right for faster running speeds with increased distance covered.

For neurons that more accurately encoded distance (Figure 8b,e), the firing fields should remain unchanged across different running speeds when plotted as a function of distance (bottom row). However, when observed as a function of time (top row), the firing fields should shift to earlier times for faster speeds as it takes less time to cover the same amount of distance if an animal is moving faster. Individual neurons exhibited variable tuning along the time-distance continuum with a majority of cells showing similar time and distance coding (Figure 8c,f), while some units showed a high selectivity to either time (Figure 8a,d) or distance (Figure 8b,e).

Next, we quantified theta phase precession slopes (rad/s) over time and distance using a similar method as before, based on the circular–linear regression between spike time and theta phase using firing fields that were in the top 80% of the peak firing rate. Theta phase of spiking activity was referenced to hippocampal theta. 18.73% of cells in the prefrontal cortex ($n = 59/315$) and 35.89% of cells in the hippocampus ($n = 75/209$) exhibited significant overall time or distance precession when we pooled together trials across all running speeds, and then calculated the precession slope for each running speed condition (25, 30, 35, 40, and 45 cm/s). To compare the

change in mean precession slopes with different running speeds across units, precession slopes were normalized to the 35 cm/s condition. We observed a significant increase in precession slope at the higher running speed of 40 cm/s in the prefrontal cortex (Wilcoxon signed-rank test, $z = 2.45$, $p = 1.43 \times 10^{-2}$). This overall effect could be related to the greater consistency of firing relative to time in the prefrontal cortex. Maintaining consistent firing relative to time could require neuronal firing to transition across phases more rapidly in the prefrontal cortex in order to maintain the size of firing fields in time. However, this does not account for the lack of effect seen at 45 cm/s (Wilcoxon signed-rank test, $z = 1.70$, $p = 8.83 \times 10^{-2}$). For slower speeds, we found no significant difference in the mean precession slope over time for the prefrontal cortex (Wilcoxon signed-rank test, 25 cm/s: $z = 0.96$, $p = .34$, 30 cm/s: $z = 0.94$, $p = .35$). For hippocampal units, the precession slope over time did not significantly change across treadmill speeds (Wilcoxon signed-rank test, 25 cm/s: $z = -0.99$, $p = .32$, 30 cm/s: $z = -0.42$, $p = .67$, 40 cm/s: $z = 0.89$, $p = .37$, 45 cm/s: $z = -0.22$, $p = .82$). Similarly, the precession slopes as a function of distance traveled also did not change for different running speeds for units in the prefrontal cortex (Wilcoxon signed-rank test, 25 cm/s: $z = 1.76$, $p = .08$, 30 cm/s: $z = 1.25$, $p = .21$, 40 cm/s: $z = 0.87$, $p = .38$, 45 cm/s: $z = 0.73$, $p = .46$) and hippocampus (Wilcoxon signed-rank test, 25 cm/s: $z = 1.05$, $p = .29$, 30 cm/s: $z = -0.74$, $p = .46$, 40 cm/s: $z = 0.56$, $p = .57$, 45 cm/s: $z = -1.37$, $p = .17$). However, there may have been too few cells that exhibit significant phase precession across different speeds for such analyses, or alternatively, there may be significant trial-to-trial variability in phase precession for individual cells (Schmidt et al., 2009).

3.8 | Neurons in both the prefrontal cortex and hippocampus are more strongly influenced by time than distance

To directly compare the relative importance of elapsed time and distance traveled on prefrontal cortex and dorsal hippocampus unit firing, we applied a generalized linear model framework. This framework allowed us to measure the consistency of a cell's firing rate at each time or distance relative to the start of the treadmill epoch, and then compare those two metrics. While many cells exhibited similar sensitivities to elapsed time and distance traveled, some cells clearly locked more tightly to one over the other (Figure 8g). Overall, ensembles in both the prefrontal cortex and hippocampus were more influenced by time than by distance traveled (Figure 8h, Wilcoxon signed-rank test, PFC: $z = 5.18$, $p = 2.17 \times 10^{-7}$, HPC: $z = 2.39$, $p = 1.68 \times 10^{-2}$). The deviance (ΔD_{T-D}) values of cells in these two regions were not significantly different, demonstrating that the influence of time over distance was equally strong across the prefrontal cortex and hippocampus (Wilcoxon rank-sum test, $z = 0.72$, $p = .47$).

4 | DISCUSSION

The experiments presented here allowed a comparison of neuronal firing patterns in both the prefrontal cortex and hippocampus during the same delay period in a delayed match to sample task. Both regions showed a distribution of neuronal firing patterns across the 8 s treadmill delay period (Figure 3a), similar to previous studies of the coding of time in the hippocampus (Kraus et al., 2013, 2015; MacDonald et al., 2011, 2013; Mau et al., 2018; Modi et al., 2014; Pastalkova et al., 2008; Salz et al., 2016; Taxidis et al., 2020) and prefrontal cortex (Bakhurin et al., 2017; Cruzado et al., 2020; Pilkiw & Takehara-Nishiuchi, 2018; Tiganj et al., 2017). This ensemble code could provide a framework for coding the time of events during a delay and the expectation of the end of the delay.

The data reveal consistent differences in the temporal distribution of neural firing between the two regions. The hippocampus contained many more discrete temporally restricted firing fields with low background activity similar to time cells described in previous work (Figure 2c), whereas the prefrontal cortex tended to show broader, more graded rate coding of time in the task (Figure 2b). This is reflected in the measure of firing sparsity in these two regions, which shows more neurons with sparse representations (discrete firing fields with lower background activity) at all time points in the hippocampus compared to the prefrontal cortex (Figure 3b). This resulted in better coding of time at low resolutions in the prefrontal cortex. While a sparse code as observed in the hippocampus may be better suited for fine discrimination of time, a denser, more distributed code as observed in the PFC is thought to provide a more efficient code such that fewer neurons are required to transmit the same information and is more precise in the presence of noise (Rigotti et al., 2013).

Consistent with the difference in sparsity, neurons in the prefrontal cortex and hippocampus showed a difference in the distribution of the slope of theta phase precession. Both regions contained some slow ramping changes in neuronal firing rate, consistent with previous studies in the hippocampus (Deadwyler & Hampson, 2004; Hampson & Deadwyler, 2003) and prefrontal cortex (Kim et al., 2013). In our data, the slow ramp-like changes were sometimes accompanied by slow changes in theta phase (Figure 6), similar to previous findings in the hippocampus and ventral striatum (Terada et al., 2017; van der Meer & Redish, 2011). However, the hippocampus showed more examples of sparse firing fields with faster theta phase precession (Figure 5e–h), especially near the start of the delay. The firing fields of time cells were remarkably stable despite changes in the treadmill running speed (Figure 8a,d). The change in treadmill speed also did not significantly change the slope of theta phase precession.

The regional difference in sparsity could reflect functional differences between the prefrontal cortex and hippocampus. A prevailing hypothesis posits that separate cortical regions process what, when, and where information, but it is in the hippocampus where these three features of experience are organized and combined into a unified representation (Eichenbaum, 2017a; Hargreaves et al., 2005). The neural circuitry responsible for the estimation of time or anticipation of future events may lie outside of the hippocampus, in cortical regions like the prefrontal cortex, which is known to be involved in planning. Thus, one could expect a more reliable global timing signal in cortical regions with activity slowly evolving across multiple

timescales. Given that firing rates of prefrontal cortex cells monotonically decay or ramp up to a salient event, this type of distributed coding mechanism may provide more information at any given time and would be synonymous with a planning or predictive function toward future behavior and action, rather than a mnemonic function that is retrospective. Sparse, sequentially activated time cells in the hippocampus fire at specific moments to stitch together a temporal record of past events but with decreasing accuracy after time has elapsed from the start of a behaviorally salient event. Because the ramping function in PFC might be more accurate than the sequential interaction of time cells in CA1, this may explain why late in the delay, prefrontal cells with monotonically changing firing rates are more temporally precise than hippocampal time cells (Figure 4e).

Memory of different events requires coding of time on multiple scales, ranging from short intervals of a few hundred milliseconds to much longer intervals of seconds, minutes, and even hours (Howard et al., 2014). A multi-scale temporal code has been simulated using a network model based on the Laplace transform and its inverse, showing how a set of neurons with exponentially decaying firing rates could be combined to generate time cells with discrete temporal firing fields over a range of seconds (Howard et al., 2014; Liu et al., 2019; Shankar et al., 2016). This computational framework is supported by the evidence that neurons coding short time intervals at the start of the delay have shorter firing fields than neurons coding longer temporal intervals (Figure 3b), consistent with previous studies (Kraus et al., 2013; Mau et al., 2018). This model predicts that temporal information is primarily coded in cells with decaying rates, similar to what we observed here in prefrontal cells, and others have found in the lateral entorhinal cortex in rodents (Tsao et al., 2018) and monkeys (Bright et al., 2020), and in the prefrontal cortex showing slow exponential decays or saturating exponential increases (Kim et al., 2013). Cells with these firing characteristics are hypothesized to transmit information, either directly or indirectly to time cells with punctate firing field properties. This model would predict that monotonically changing activity would be both necessary for, as well as more temporally precise than time cell activity. While the role of the entorhinal cortex input to hippocampal time cells is supported by previous studies, those results do not preclude a prefrontal timing signal as well. Indeed, time cells remained even after the inactivation of the medial entorhinal cortex, albeit to a lesser degree (Robinson et al., 2017). Together with previous studies, these results suggest that hippocampal time cells may receive temporal information from cortical regions and transform decaying activity into sparse time fields using a Laplace transform (Howard et al., 2014; Liu et al., 2019).

This model based on the Laplace transform can also be used to simulate theta phase coding and generate the difference between fast theta phase precession with steep slopes in small firing fields to slow theta phase precession with shallow slopes in cells with long ramp-like firing fields (Shankar et al., 2016, Figures 5 and 6). The robustness of theta phase to changes in running speed could reflect selective coding focused on the 8 s time interval, despite the change in distance of running (Figure 8). The difference between the prefrontal cortex and hippocampus could reflect a broader time scale prediction by prefrontal cortex that focuses on the behavioral time scale of reward prediction (Shankar et al., 2016), similar to the ramping activity during the time interval approaching reward seen in the striatum, which may be mediated by neuromodulators such as dopamine (van der Meer & Redish, 2011).

As an alternative interpretation, the higher resolution and discrete coding of time and space in the hippocampus could interact with a reinforcement learning mechanism in the prefrontal cortex (Hasselmo & Eichenbaum, 2005). In this framework, the prefrontal cortex might not represent the episodic memory of time and space but instead represents the value of specific states or actions, as in the value function or state-action value function in reinforcement learning theory (Sutton & Barto, 1998). For example, the ramp-like increase in activity in some prefrontal cells could reflect the increase in value of states (different time points) as the delay progresses and the response and reward get closer in time, similar to the proposal for the ventral striatum (van der Meer & Redish, 2011).

Furthermore, the interaction of prefrontal cortex and hippocampus may reflect the complex dynamics of a phase code from the hippocampus interacting with a decision process in the prefrontal cortex. The phase code in the hippocampus might reflect coding of sequences of activity that encode and retrieve segments of the spatiotemporal trajectory of the task, as found in the evidence of theta sequence readout in the hippocampus (Foster & Wilson, 2007; Terada et al., 2017). These spatiotemporal sequences do not necessarily only involve sequences of place cells and time cells, but could also involve sequences that include representations of the objects, behavioral responses, and reward value (Maurer et al., 2012; Terada et al., 2017; Wiener et al., 1989). The phase coding in prefrontal cortex may reflect timing of decision processes in different contexts relative to theta rhythm oscillations, as shown by changes in prefrontal cortical phase of firing during different task demands (Hyman et al., 2005; Jones & Wilson, 2005b).

In summary, the data presented here indicate clear differences in neuronal responses during a temporal delay in the prefrontal cortex versus hippocampus, with prefrontal cortex exhibiting more ramping activity and less sparse coding by time cells relative to the hippocampus. Consistent with this, prefrontal cortex shows greater temporal precision for decoding of time at long time lags and the hippocampus exhibits faster transitions in theta phase with time. As discussed above, these differences could reflect complementary roles of the prefrontal cortex and hippocampus in the coding of time for the performance of memory-guided behavior.

AUTHOR CONTRIBUTIONS

Wing Ning, John H. Bladon, and Michael E. Hasselmo designed the experiments. Wing Ning and John H. Bladon performed research. Wing Ning and John H. Bladon analyzed the data. Wing Ning, John H. Bladon, and Michael E. Hasselmo wrote the paper.

ACKNOWLEDGMENTS

We would like to thank Sophie M. Steinwenter, Jiawen Chen, Blake A. Fordyce, Taylor Feaster, and Humna Siddiqi for technical assistance with behavioral training. The authors also thank Dr Andrew

S. Alexander for useful discussions during data analysis and early manuscript preparation, Daniel Orlin, Jun Shen, and Denise Parisi for administrative support, Dr Marc W. Howard and all members of the Eichenbaum and Hasselmo labs for helpful discussions and close support. This research was funded by the U.S. National Institutes of Health R01 MH052090, R01 MH060013, R01 MH095297, R01 MH120073 and the U.S. Office of Naval Research DURIP N00014-17-1-2304, MURI N00014-16-1-2832, and MURI N00014-19-1-2571.

CONFLICT OF INTEREST

The authors declare no conflicts of interest.

DATA AVAILABILITY STATEMENT

Data and custom MATLAB code used for data analysis can be made available upon request.

ORCID

Wing Ning https://orcid.org/0000-0002-7083-0558
John H. Bladon https://orcid.org/0000-0001-8993-9898
Michael E. Hasselmo https://orcid.org/0000-0002-9925-6377

REFERENCES

Akhlaghpour, H., Wiskerke, J., Choi, J. Y., Taliaferro, J. P., Au, J., & Witten, I. B. (2016). Dissociated sequential activity and stimulus encoding in the dorsomedial striatum during spatial working memory. *eLife*, *5*, e19507.

Bakhurin, K. I., Goudar, V., Shobe, J. L., Claar, L. D., Buonomano, D. V., & Masmanidis, S. C. (2017). Differential encoding of time by prefrontal and striatal network dynamics. *The Journal of Neuroscience*, *37*, 854–870.

Batschelet, E. (1981). *Circular statistics in biology*. Academic Press.

Belluscio, M. A., Mizuseki, K., Schmidt, R., Kempter, R., & Buzsáki, G. (2012). Cross-frequency phase-phase coupling between theta and gamma oscillations in the hippocampus. *Journal of Neuroscience*, *32*, 423–435.

Berens, P. (2009). CircStat: A MATLAB toolbox for circular statistics. *Journal of Statistical Software*, *31*, 1–21.

Bright, I. M., Meister, M. L. R., Cruzado, N. A., Tiganj, Z., Buffalo, E. A., & Howard, M. W. (2020). A temporal record of the past with a spectrum of time constants in the monkey entorhinal cortex. *Proceedings of the National Academy of Sciences of the United States of America*, *117*, 20274–20283.

Cruzado, N. A., Tiganj, Z., Brincat, S. L., Miller, E. K., & Howard, M. W. (2020). Conjunctive representation of what and when in monkey hippocampus and lateral prefrontal cortex during an associative memory task. *Hippocampus*, *30*, 1332–1346.

Deadwyler, S. A., & Hampson, R. E. (2004). Differential but complementary mnemonic functions of the hippocampus and subiculum. *Neuron*, *42*, 465–476.

Dombeck, D. A., Harvey, C. D., Tian, L., Looger, L. L., & Tank, D. W. (2010). Functional imaging of hippocampal place cells at cellular resolution during virtual navigation. *Nature Neuroscience*, *13*, 1433–1440.

Dragoi, G., & Buzsáki, G. (2006). Temporal encoding of place sequences by hippocampal cell assemblies. *Neuron*, *50*, 145–157.

Eichenbaum, H. (2017a). On the integration of space, time, and memory. *Neuron*, *95*, 1007–1018.

Eichenbaum, H. (2017b). Prefrontal-hippocampal interactions in episodic memory. *Nature Reviews. Neuroscience*, *18*, 547–558.

Eichenbaum, H., & Fortin, N. J. (2003). Episodic memory and the hippocampus: It's about time. *Current Directions in Psychological Science*, *12*, 53–57.

Fisher, N. I. (1995). *Statistical analysis of circular data*. Cambridge University Press.

Foster, D. J., & Wilson, M. A. (2007). Hippocampal theta sequences. *Hippocampus*, *17*, 1093–1099.

Hampson, R. E., & Deadwyler, S. A. (2003). Temporal firing characteristics and the strategic role of subicular neurons in short-term memory. *Hippocampus*, *13*, 529–541.

Hargreaves, E. L., Rao, G., Lee, I., & Knierim, J. J. (2005). Major dissociation between medial and lateral entorhinal input to dorsal hippocampus. *Science*, *308*, 1792–1794.

Hasselmo, M. E. (2012). *How we remember: Brain mechanisms of episodic memory*. MIT Press.

Hasselmo, M. E., & Eichenbaum, H. (2005). Hippocampal mechanisms for the context-dependent retrieval of episodes. *Neural Networks*, *18*, 1172–1190.

Howard, M. W., MacDonald, C. J., Tiganj, Z., Shankar, K. H., Du, Q., Hasselmo, M. E., & Eichenbaum, H. (2014). A unified mathematical framework for coding time, space, and sequences in the hippocampal region. *The Journal of Neuroscience*, *34*, 4692–4707.

Huxter, J., Burgess, N., & O'Keefe, J. (2003). Independent rate and temporal coding in hippocampal pyramidal cells. *Nature*, *425*, 828–832.

Hyman, J. M., Zilli, E. A., Paley, A. M., & Hasselmo, M. E. (2005). Medial prefrontal cortex cells show dynamic modulation with the hippocampal theta rhythm dependent on behavior. *Hippocampus*, *15*, 739–749.

Jeewajee, A., Barry, C., Douchamps, V., Manson, D., Lever, C., & Burgess, N. (2013). Theta phase precession of grid and place cell firing in open environments. *Philosophical Transactions of the Royal Society of London. Series B, Biological Sciences*, *369*, 20120532.

Jones, M. W., & Wilson, M. A. (2005a). Phase precession of medial prefrontal cortical activity relative to the hippocampal theta rhythm. *Hippocampus*, *15*, 867–873.

Jones, M. W., & Wilson, M. A. (2005b). Theta rhythms coordinate hippocampal–prefrontal interactions in a spatial memory task. *PLoS Biology*, *3*, e402.

Jung, M. W., Wiener, S. I., & McNaughton, B. L. (1994). Comparison of spatial firing characteristics of units in dorsal and ventral hippocampus of the rat. *Journal of Neuroscience*, *14*, 7347–7356.

Kempter, R., Leibold, C., Buzsaki, G., Diba, K., & Schmidt, R. (2012). Quantifying circular-linear associations: Hippocampal phase precession. *Journal of Neuroscience Methods*, *207*, 113–124.

Kim, J., Ghim, J.-W., Lee, J. H., & Jung, M. W. (2013). Neural correlates of interval timing in rodent prefrontal cortex. *The Journal of Neuroscience*, *33*, 13834–13847.

Kim, S. M., Ganguli, S., & Frank, L. M. (2012). Spatial information outflow from the hippocampal circuit: Distributed spatial coding and phase precession in the subiculum. *The Journal of Neuroscience*, *32*, 11539–11558.

Kjelstrup, K. B., Solstad, T., Brun, V. H., Hafting, T., Leutgeb, S., Witter, M. P., Moser, E. I., & Moser, M. B. (2008). Finite scale of spatial representation in the hippocampus. *Science*, *321*, 140–143.

Kraus, B. J., Brandon, M. P., Robinson, R. J., II, Connerney, M. A., Hasselmo, M. E., & Eichenbaum, H. (2015). During running in Place, grid cells integrate elapsed time and distance run. *Neuron*, *88*, 578–589.

Kraus, B. J., Robinson, R. J., II, White, J. A., Eichenbaum, H., & Hasselmo, M. E. (2013). Hippocampal "time cells": Time versus path integration. *Neuron*, *78*, 1090–1101.

Liu, Y., Tiganj, Z., Hasselmo, M. E., & Howard, M. W. (2019). A neural microcircuit model for a scalable scale-invariant representation of time. *Hippocampus*, *29*, 260–274.

MacDonald, C. J., Carrow, S., Place, R., & Eichenbaum, H. (2013). Distinct hippocampal time cell sequences represent odor memories in immobilized rats. *The Journal of Neuroscience*, *33*, 14607–14616.

MacDonald, C. J., Lepage, K. Q., Eden, U. T., & Eichenbaum, H. (2011). Hippocampal "time cells" bridge the gap in memory for discontiguous events. *Neuron*, *71*, 737–749.

Mau, W., Sullivan, D. W., Kinsky, N. R., Hasselmo, M. E., Howard, M. W., & Eichenbaum, H. (2018). The same hippocampal CA1 population simultaneously codes temporal information over multiple timescales. *Current Biology*, *28*, 1499–1508.e1494.

Maurer, A. P., Burke, S. N., Lipa, P., Skaggs, W. E., & Barnes, C. A. (2012). Greater running speeds result in altered hippocampal phase sequence dynamics. *Hippocampus*, *22*, 737–747.

Mello, G. B. M., Soares, S., & Paton, J. J. (2015). A scalable population code for time in the striatum. *Current Biology*, *25*, 1113–1122.

Modi, M. N., Dhawale, A. K., & Bhalla, U. S. (2014). CA1 cell activity sequences emerge after reorganization of network correlation structure during associative learning. *eLife*, *3*, e01982.

O'Keefe, J., & Burgess, N. (2005). Dual phase and rate coding in hippocampal place cells: Theoretical significance and relationship to entorhinal grid cells. *Hippocampus*, *15*, 853–866.

O'Keefe, J., & Dostrovsky, J. (1971). The hippocampus as a spatial map. Preliminary evidence from unit activity in the freely-moving rat. *Brain Research*, *34*(1), 171–175.

O'Keefe, J., & Recce, M. L. (1993). Phase relationship between hippocampal place units and the EEG theta rhythm. *Hippocampus*, *3*, 317–330.

Olypher, A. V., Lansky, P., Muller, R. U., & Fenton, A. A. (2003). Quantifying location-specific information in the discharge of rat hippocampal place cells. *Journal of Neuroscience Methods*, *127*, 123–135.

Pastalkova, E., Itskov, V., Amarasingham, A., & Buzsaki, G. (2008). Internally generated cell assembly sequences in the rat hippocampus. *Science*, *321*, 1322–1327.

Paxinos, G., & Watson, C. (1998). *The rat brain in stereotaxic coordinates*. Academic Press.

Pilkiw, M., & Takehara-Nishiuchi, K. (2018). Neural representations of time-linked memory. *Neurobiology of Learning and Memory*, *153*, 57–70.

Rigotti, M., Barak, O., Warden, M. R., Wang, X.-J., Daw, N. D., Miller, E. K., & Fusi, S. (2013). The importance of mixed selectivity in complex cognitive tasks. *Nature*, *497*, 585–590.

Robinson, N. T. M., Priestley, J. B., Rueckemann, J. W., Garcia, A. D., Smeglin, V. A., Marino, F. A., & Eichenbaum, H. (2017). Medial entorhinal cortex selectively supports temporal coding by hippocampal neurons. *Neuron*, *94*, 677–688.

Royer, S., Sirota, A., Patel, J., & Buzsaki, G. (2010). Distinct representations and theta dynamics in dorsal and ventral hippocampus. *The Journal of Neuroscience*, *30*, 1777–1787.

Salz, D. M., Tiganj, Z., Khasnabish, S., Kohley, A., Sheehan, D., Howard, M. W., & Eichenbaum, H. (2016). Time cells in hippocampal area CA3. *The Journal of Neuroscience*, *36*, 7476–7484.

Schmidt, R., Diba, K., Leibold, C., Schmitz, D., Buzsaki, G., & Kempter, R. (2009). Single-trial phase precession in the hippocampus. *The Journal of Neuroscience*, *29*, 13232–13241.

Schmitzer-Torbert, N., Jackson, J., Henze, D., Harris, K., & Redish, A. D. (2005). Quantitative measures of cluster quality for use in extracellular recordings. *Neuroscience*, *131*, 1–11.

Shankar, K. H., Singh, I., & Howard, M. W. (2016). Neural mechanism to simulate a scale-invariante future. *Neural Computation*, *28*, 2594–2627.

Shimbo, A., Izawa, E. I., & Fujisawa, S. (2021). Scalable representation of time in the hippocampus. Science. *Advances*, *7*, eabd7013.

Skaggs, W. E., McNaughton, B. L., Gothard, K. M. & Markus, E. J. (1993). An information-theoretic approach to deciphering the hippocampal code. *Advances in Neural Information Processing Systems*, *5*, 1030–1037.

Skaggs, W. E., McNaughton, B. L., Wilson, M. A., & Barnes, C. A. (1996). Theta phase precession in hippocampal neuronal populations and the compression of temporal sequences. *Hippocampus*, *6*, 149–172.

Sutton, R. S., & Barto, A. G. (1998). *Reinforcement learning: An Introduction*. MIT Press.

Takahashi, M., Nishida, H., Redish, A. D., & Lauwereyns, J. (2014). Theta phase shift in spike timing and modulation of gamma oscillation: A dynamic code for spatial alternation during fixation in rat hippocampal area CA1. *Journal of Neurophysiology*, *111*, 1601–1614.

Taxidis, J., Pnevmatikakis, E. A., Dorian, C. C., Mylavarapu, A. L., Arora, J. S., Samadian, K. D., Hoffberg, E. A., & Golshani, P. (2020). Differential emergence and stability of sensory and temporal representations in context-specific hippocampal sequences. *Neuron*, *108*, 984–998.

Terada, S., Sakurai, Y., Nakahara, H., & Fujisawa, S. (2017). Temporal and rate coding for discrete event sequences in the hippocampus. *Neuron*, *94*, 1248–1262.e4.

Tiganj, Z., Jung, M. W., Kim, J., & Howard, M. W. (2017). Sequential firing codes for time in rodent medial prefrontal cortex. *Cerebral Cortex*, *27*, 5663–5671.

Tingley, D., Alexander, A. S., Quinn, L. K., Chiba, A. A., & Nitz, D. (2018). Multiplexed oscillations and phase rate coding in the basal forebrain. *Science Advances*, *4*, eaar3230.

Tsao, A., Sugar, J., Lu, L., Wang, C., Knierim, J. J., Moser, M. B., & Moser, E. I. (2018). Integrating time from experience in the lateral entorhinal cortex. *Nature*, *561*, 57–62.

Tulving, E. (1983). *Elements of episodic memory*. Oxford University Press.

Umbach, G., Kantak, P., Jacobs, J., Kahana, M., Pfeiffer, B. E., Sperling, M., & Lega, B. (2020). Time cells in the human hippocampus and entorhinal cortex support episodic memory. *Proceedings of the National Academy of Sciences of the United States of America*, *117*, 28463–28474.

van der Meer, M. A. A., & Redish, A. D. (2011). Theta phase precession in rat ventral striatum links place and reward information. *The Journal of Neuroscience*, *31*, 2843–2854.

Wiener, S. I., Paul, C. A., & Eichenbaum, H. (1989). Spatial and behavioral correlates of hippocampal neuronal activity. *The Journal of Neuroscience*, *9*, 2737–2763.

Zar, J. H. (1999). *Biostatistical analysis* (4th ed., pp. 230–241). Prentice-Hall.

How to cite this article: Ning, W., Bladon, J. H., & Hasselmo, M. E. (2022). Complementary representations of time in the prefrontal cortex and hippocampus. *Hippocampus*, *32*(8), 577–596. https://doi.org/10.1002/hipo.23451